ELSEVIER

Marine and Petroleum Geology 20 (2003) 911–933

Marine and Petroleum Geology

www.elsevier.com/locate/marpetgeo

Modelling subaqueous bipartite sediment gravity flows on the basis of outcrop constraints: first results

Roberto Tinterri[a], Michele Drago[b], Alberto Consonni[c], Giancarlo Davoli[c,*], Emiliano Mutti[a]

[a]*Dipartimento di Scienze della Terra, University of Parma, Parco Area delle Scienze 157/A, 43100 Parma, Italy*
[b]*ENI—Snamprogetti S.p.A., Via Toniolo no. 1, 61032 Fano, Italy*
[c]*ENI—Exploration and Production Division, Via Emila no. 1, San Donato Milanese 20097, Italy*

Received 1 September 2002; accepted 3 March 2003

Abstract

This paper presents the first attempt to provide a two-dimensional numerical model simulating processes and related deposits of individual subaqueous bipartite gravity flows. A new code for dense flows has been implemented and coupled with a code for turbulent flows. An integrated approach has been adopted: the numerical model is constrained by detailed facies tract analysis of outcropping ancient turbidites, and by grain-size analyses performed on the individual component facies. The results presented here illustrate the ability of the coupled model to simulate with good accuracy both the dense and turbulent flows and the related deposits. Particularly, the model can reproduce grain-size distributions comparable to those measured from the ancient turbidites.

Keywords: Numerical modelling; Genetic facies tract; Bipartite flows

1. Introduction

In recent years, hydrocarbon exploration on continental margins has moved to progressively deeper waters with similarly increasing costs. Most of the risks inherent to this exploratory effort are mainly related to the unexpected complexity of these basins as revealed by three-dimensional (3D) seismic surveys, subbottom profiles and side-scan sonar studies. The seascape, as well as the architecture of buried basins, have shown new scenarios for deep-water clastic sedimentation, which cast serious doubts on the relevance of classic sedimentation models developed over many years by sedimentologists.

In particular, this new scenario shows that turbidite depositional systems of slope and base-of-slope regions are considerably more complex than described by current deep-sea models. In order to lower exploration risks, in recent years a great deal of effort has been directed toward developing new predictive models of turbidite sand deposition mainly based on the understanding of the physical processes governing transportation and deposition of turbidity currents and, more generally, submarine sediment gravity flows.

Facies studies on sediment gravity flow deposits clearly demonstrate that in proximal zones they are characterised by coarse-grained graded, massive sediments interpreted to be the deposits of inertial dense flows (*sensu* Norem, Locat, & Schieldrop, 1990; see also Mutti, Tinterri, Benevelli, di Biase, and Cavanna (2003)), which are replaced, in distal zones, by finer-grained laminated deposits related to dilute turbulent flows (Bouma, 1962; Lowe, 1982; Mutti, 1992; Sanders, 1965). These sediments are therefore consistent with deposition from bipartite flows characterised by a basal dense flow and an overlying more dilute turbulent one (Sanders, 1965), possibly derived from the progressive downcurrent transformation (in the sense of Fisher (1983)) of the basal flow (Mutti et al., 1999; Norem et al., 1990; Ravenne & Beghin, 1983).

As recently pointed out by Peakall, Felix, McCaffrey, and Kneller (2001) and Tinterri and Consonni (2001), research on gravity flows has largely been based on single flow-types and using a single research approach. In particular, these flows and their deposits have been studied through both laboratory experiments and numerical modelling with very limited support from field data. Several authors have carried out

* Corresponding author. Tel.: +39-2-52061520.
E-mail address: giancarlo.davoli@agip.it (G. Davoli).

0264-8172/$ - see front matter © 2003 Elsevier Ltd. All rights reserved.
doi:10.1016/j.marpetgeo.2003.03.003

studies on both dense inertial flows and dilute turbulent flows, mainly based on flume experiments (Chen, 1997; Kneller & Buckee, 2000; Middleton, 1993; Simpson, 1997; with references therein). Recently, for example, Iverson (1997), Parsons, Whipple, and Simoni (2001) and Takahashi (1991) performed experimental works on subaerial dense flows, whereas Kneller (1995), Marr, Harff, Shanmugam, and Parker (2001), Mohrig and Marr (2003), Mohrig, Whipple, Hondzo, Ellis, and Parker, 1998 and Postma, Nemec, and Kleinsphein (1988), concentrated on subaqueous sediment gravity flows. These papers provide important information about flow dynamics, but are affected by a physical scale problem intrinsic to the flume approach itself. In addition, most of the flume experiments are carried out using only very-fine grain sizes. In other words, it is difficult to scale the results of these experiments to real sediment gravity flows, travelling tens of kilometres and transporting/depositing huge volumes of sediment.

Other authors approached the study of gravity flows through the development of numerical models (Drago & Terenzi, 2001; Felix, 2001, 2002; Imran, Harff, & Parker, 2001; Iverson, 1997; Mulder, Savoye, & Syvitski, 1997; Pratson, Imran, Hutton, Parker, & Syvitsky, 2001; Reed, Niedoroda, Dalton, & Parker, 2000; Takahashi, 1991, 2001; Zeng & Lowe, 1997a,b). However, very few authors tried to couple numerical models of different flow types in order to provide a more complete description of the downcurrent flow transformations and sediment distribution (see, for example, Drago (2002), on the transition from a cohesive debris flow to a turbulent flow).

Field work and subsurface bottom core studies of ancient turbidite systems allow the direct observation of natural large-scale gravity flow deposits (and the inference of the related processes from sedimentary structures). Unfortunately, field work is a highly time-consuming approach, and consequently, basinwide-scale detailed sedimentologic works are very rare (see, for example, Remacha and Fernandez (2003)); on the other hand, bottom core recovery is very expensive, and cored wells are generally few or too widely spaced with respect to the size of the turbidite system to be studied.

According to Peakall et al. (2001) (see also Tinterri and Consonni (2001)), significant improvements in the understanding of gravity flow dynamics can be achieved through different research approaches. In this paper, we attempt to develop a numerical modelling of sediment gravity flows and their deposits based on the constraints of very detailed stratigraphic and facies analysis carried out in the Eocene foreland basins of the south central Pyrenees. The facies tract reconstructed for these studies covers a distance of some 120 km parallel to paleocurrent direction. Evidentially, coeval individual beds and packets of beds show a very distinct downcurrent facies change from the deposit of a dense and relatively coarse-grained flow, in which excess pore pressures are interpreted as the key to mobility, to the deposit of a more dilute turbulent flow where finer grained particles are entirely transported as suspended load. The process has been discussed by Ravenne and Beghin (1983) and Norem et al. (1990); the resulting sediments have been described in detail by Mutti et al. (1999). Based on these assumptions, we attempt here to provide a two-dimensional (2D) numerical model able to simulate the downcurrent evolution of individual bipartite flows and of their deposits, in order to help improve the prediction of their extent and spatial change in grain-size distribution.

The present paper illustrates the first results of a research project carried on by ENI in collaboration with the University of Parma, through a strict collaboration between field sedimentologists and physicists (cf. Tinterri & Consonni, 2001).

2. Methodology

The flow diagram of Fig. 1 shows the methodology adopted in the present work and summarised as follows: (1) choosing of the bed to be modelled through a high-resolution bed by bed correlation framework (Fig. 2); (2) detailed facies analysis of the bed; (3) inference of the physical processes and so of the main particle support mechanisms; (4) construction of a physical model on the basis of the field inferences and literature data; (5) construction of a mathematical model for the numerical simulation; (6) numerical reproduction of the bed. Following this methodology the mathematical model is linked to a physical model strictly derived by a detailed facies analysis of the bed.

The sedimentologic approach used in these notes is based on the process-oriented ‘facies tract’ concept (Lowe, 1982; Mutti, 1992). The facies tract is the association of genetically related facies types which record, within each considered system, the downstream evolution of a sediment gravity flow. The ideal facies tract is recorded by a bed deposited by a single sediment gravity flow undergoing transformations during its basinward motion. In these terms, the concept of gravity-flow facies can be applied to a specific depositional division (i.e. lamina or laminaset, *sensu* Campbell, 1967). A turbidite facies therefore represents the deposit of a gravity flow at a specific location along the path of the flow, whereas a facies tract represents the whole of the facies deposited by a single gravity flow. So, within a bed, the vertical facies association represents how the flow conditions change in time at a fixed location; the horizontal facies association records how the flow conditions change in space through successive flow transformations. This approach implies that, for each considered turbidite system, facies tracts must be established on the basis of detailed stratal correlation patterns.

The foreland Hecho Group turbidite complex (Eocene, south central Pyrenees) has been studied extensively by Mutti and co-workers (Mutti, 1971; Mutti et al., 1985; Mutti, Seguret & Zavala, 1988; Mutti et al., 1999; Remacha & Fernandez, 2003; Remacha et al., 1998), so

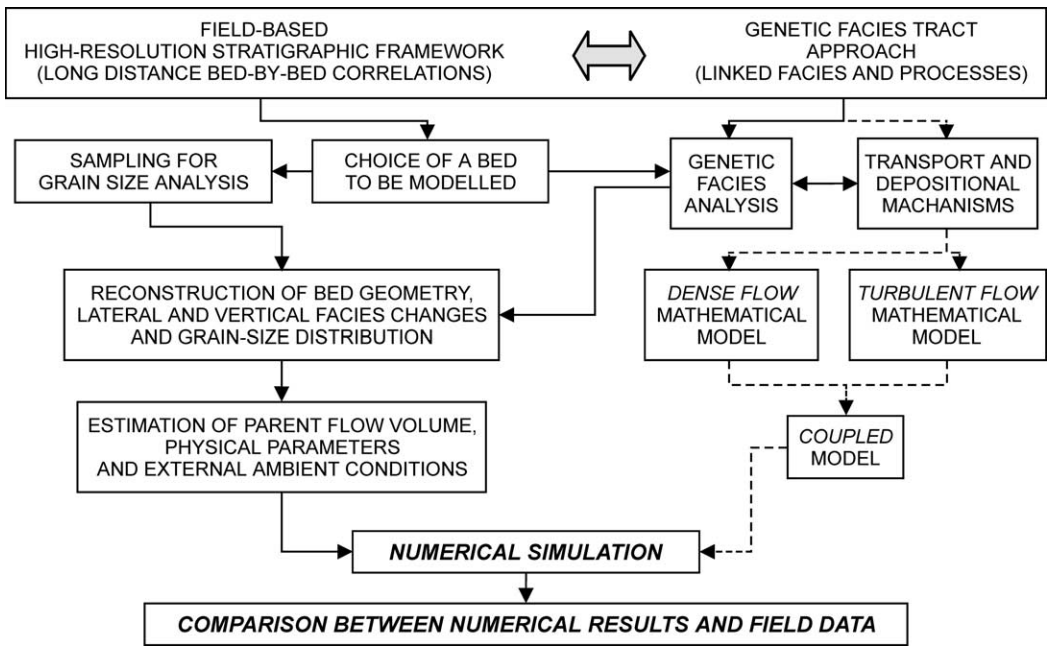

Fig. 1. Workflow diagram summarising the methodology adopted in this study. On the left side, solid lines represent the 'field geology path'; on the right, dashed lines represent the 'physics/mathematic path'.

that high-resolution bed-by-bed correlations are presently available throughout most of the outcropping succession, over distances up to tens of kilometres. For the purposes of the current project, seven beds of the Banaston and Broto turbidite systems have been studied in detail and sampled for grain-size studies (for a total of 125 collected samples). Facies analysis has been carried out following the genetic facies classification proposed by Mutti et al. (2003, with references therein).

In this study, the modelling of a single bed from the Broto system is presented. The bed, whose facies tract records the downcurrent transition between dense flow and turbulent flow deposits, is framed within a 30-m thick stratigraphic interval described in detail at four different locations (Fig. 2). This interval is in turn framed within a regional-scale high-resolution stratigraphic framework based on works by Remacha (1983) and Remacha (1998, unpublished data). The bed has been sampled facies-by-facies in order to carry out grain-size analyses and to characterise each facies in terms of grain-size populations. Grain-size analyses have been performed at the ENI Laboratory using a SYMPATEC laser diffractometer (range of measurement is 0.9–1750 μm). Petrographic and XRD analyses have been carried out in order to evaluate the mineralogical composition and the cement and clay content.

The geometry, the facies tract and the grain-size distribution of the bed have been restored by integrating facies analysis and grain-size results. Extrapolations have been made in order to characterise the bed beyond the measured field sections (downcurrent and immediately upcurrent). Decisions on how to extend the bed in its most distal position have made using field measurements by Mutti (1971).

The next step has been the estimation of the parent flow volume and physical parameters (e.g. bulk viscosity, bulk density, bed friction angle, etc.) as well as the evaluation of the external ambient conditions (bathymetry and sea bottom roughness).

On the mathematical side, both papers selected from the available literature (see details in Section 4) and field constraints, contributed to create ex novo a physical model for dense overpressured flows; for turbulent flows, a physical model previously carried out by Drago and Terenzi (2001) has been used. The two models, which work independently, have been coupled in order to simulate the downcurrent transition between dense overpressured and turbulent flow conditions, both in terms of processes and deposits. The input conditions for the numerical simulations have been derived from facies and grain-size analyses.

Finally, the numerical results have been compared with the field data in order to check the reliability of the model and of the initial assumptions made for the run. The comparison may also help to give insight into transport and depositional processes of still poorly understood facies.

3. Sedimentological framework

3.1. Facies and processes of bipartite sediment gravity flows

Gravity flows are generally classified using a fourfold scheme based on the main particle support mechanisms:

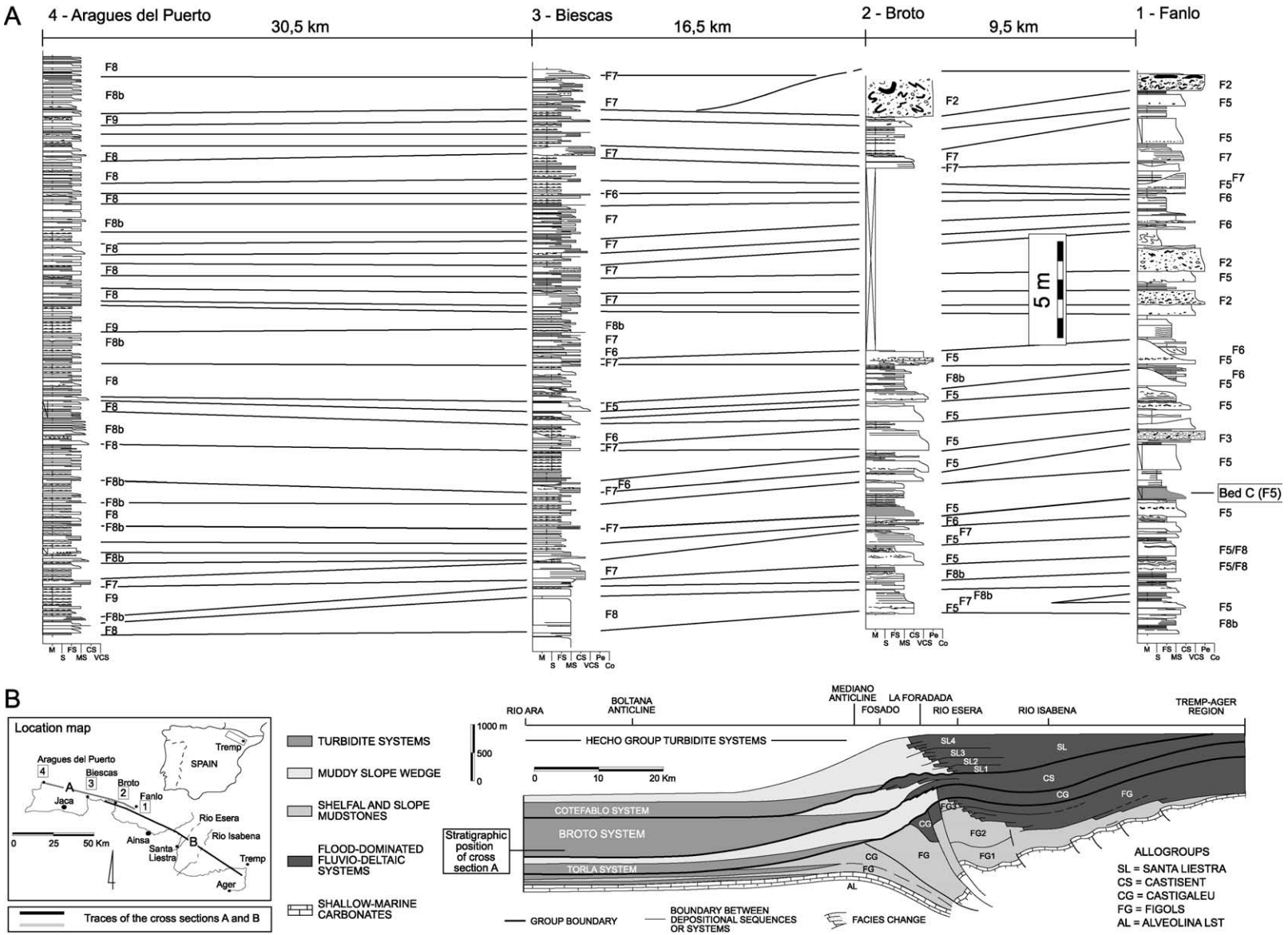

Fig. 2. Stratigraphic interval studied in detail within the Broto turbidite system (cross-section A), from proximal zone (Fanlo 1) to distal zone (Aragues del Puerto 4) (Hecho Group, Eocene, south central Pyrenees). The bed C selected to be modelled is labelled on the diagram. The interval is traced regionally across the Broto turbidite system on the basis of the high-resolution stratigraphic framework of Remacha (1983) and Remacha (1998, unpublished data). Detailed facies analysis has been carried out on the basis of the classification proposed by Mutti et al. (2003, see Fig. 3). The crudely laminated (banded) F8 deposits described in Section 3.1 are highlighted through the code F8b. Cross-section B (from Mutti et al. (1999)) gives the regional geologic framework.

matrix strength, dispersive pressure, escaping pore fluid and turbulence (Middleton & Hampton, 1973). Actually, using the process-oriented 'facies tract' approach it should be assumed that every gravity flow is a hybrid flow characterised by different parts with different mechanical behaviour, each of which causes the deposition of a specific type of facies (Tinterri & Consonni, 2001); within every part, two or more particle support mechanisms and thus momentum-transporting processes can coexist. In general, two end members of sediment gravity flows can be distinguished: (1) dense flows and (2) turbulent flows.

Following Mutti et al. (1999), each of these types of gravity flow is assumed to transport well defined grain-size populations as distinct entities, thus forming similarly distinct facies groups. On the basis of detailed facies analyses, grain-size populations can be divided in four dynamic classes that are: (A) boulder- to small pebble-sized clasts, (B) small pebbles to coarse sand, (C) medium sand and (D) fine sand to mud (Fig. 3). In this way, the different parts of a sediment gravity flow are characterised by distinctive mechanical behaviours and grain-size populations. In general, the dense parts, which are characterised by an interaction of matrix strength, intergranular collisions and overpressure, will be able to transport the coarser grain-size populations A, B and part of C; the dilute parts, principally characterised by turbulence, will tend to transport the finer grain-size populations D and, possibly, part of C (Figs. 3 and 4).

The main facies tract observed along the axis of a foredeep basin and its interpretation in terms of bipartite sediment gravity flow deposits are shown in Figs. 3 and 4, respectively. A full discussion on the origin and dynamic evolution of these flows and their deposits is beyond the scope of this paper; the reader is referred to the exhaustive works by Mutti et al. (2003, 1999) and Normark and Piper (1991) with references therein. However, two key points have to be kept in mind for the purposes of this paper: (1) clear evidences from both modern and ancient marine basins suggest that flood-generated hyperpycnal flows can play a major role in the origin of turbidity currents (Milliman & Syvitski, 1992; Mulder & Syvitski, 1995; Mulder, Syvitski, & Skene, 1998; Mutti, Davoli, Tinterri & Zavala, 1996; Mutti et al., 2000) and (2) most of the flood-related deep-water sediment gravity flows can be interpreted as originating from dense overpressured flows which soon become bipartite (Mutti et al., 1999). As indicated by the literature, however, other processes are able to produce a bipartite flow. In particular, gravity transformations (Postma et al., 1988), rate of fallout and mud contents (Lowe & Guy, 2000) may play an important role in generating a bipartite flow from a high-density turbulent flow; it is the case of reconcentration phenomenons occurring at the river mouth in flood-related hyperpycnal flows (Mutti et al., 2003, cf. also with McLeod, Carey, and Sparks (1999)) or in waning turbidity currents after a hydraulic jump (Kneller & Branney, 1995; Mutti, 1992). In fact, due to the rate of flow deceleration, rate of fallout and mud content, in these cases a basal dense flow can form through en masse deposition (Middleton, 1993 with references; see also Banerjee (1977)) or through the progressive rise of the sedimentation interface, with the possibility to generate a viscous cohesive sublayer tens of dm-thick (Lowe & Guy, 2000; see also Kneller and Branney (1995), Vrolijk and Southard (1997)). These processes, which may play an important role in the downcurrent evolution of a sediment gravity flow, are taken into account in the numerical modelling recently proposed by Felix (2001, 2002). Nevertheless, field and theoretical evidences tend to favour the dense overpressured hypothesis for the case presented here. This modelling, therefore, is based on the assumption that the turbulent flow is generated by the elutriation processes of the trailing edge and by the transformation of the leading edge of the basal dense flow (i.e. the dense flow gives rise to the turbulent flow and not vice versa).

In this way, bipartite flows include a faster-moving, basal and denser inertial flow, where turbulence is damped by high sediment concentration, and an upper more dilute turbulent flow. These two types of gravity flow are responsible for the deposition of poorly sorted massive facies (F2, F3 and F5) and well sorted laminated facies (F9), respectively (Fig. 4). As pointed out by Norem et al. (1990) for subaqueous sediment gravity flows and Iverson (1997) for subaerial debris flows, the long runout distances of the basal dense flow, also testified by the large extension of massive facies in ancient deposits (Mutti et al., 1999; Remacha & Fernandez, 2003; see also Fig. 2), can only be explained by assuming that a substantial excess pore pressure, which tends to reduce the internal friction, was present within the flow.

During its downslope motion (Fig. 4a) the gravelly basal dense flow tends to segregate the coarser grain-size populations at the leading edge of the flow (Mutti et al., 1999; Sanders, 1965), where the increase of permeability causes a decrease of pore-fluid pressure and the consequent increase of intergranular friction. At the same time, the high shear stress exerted by the ambient fluid and the fluidisation processes related to water injections at the base of the flow front, tend to transform the frontal part of the flow and to generate turbulence (Marr et al., 2001; Morhig & Marr, 2002; Mohrig, Whipple, Hondzo, Ellis, & Parker, 1998; Mutti et al., 1999). Therefore, the basal gravelly dense flow can be interpreted as a composite gravity flow characterised by (1) a body in which the pore fluid pressure, sufficient to cause liquefaction, is developed and maintained during mobilisation and motion of the flow and (2) a head in which the grain-contact friction and the bed friction will cause the deposition of the frontal part of the flow (F3 deposits, Fig. 4b). During this phase the finer grain-size populations, which were being transported in the trailing edge of the flow, can overtake the newly formed deposit and keep moving downcurrent, producing another finer composite

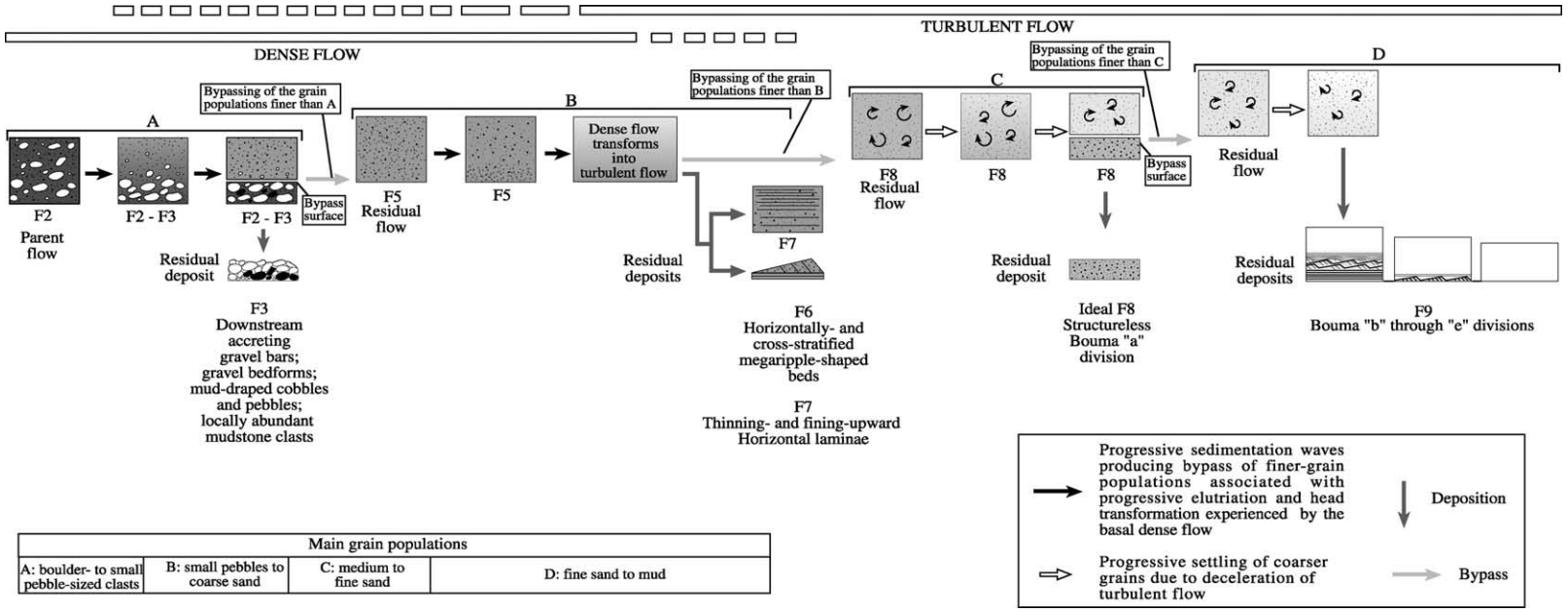

Fig. 3. Facies and inferred processes associated with a highly efficient turbidity current (from Mutti et al. (2003)).

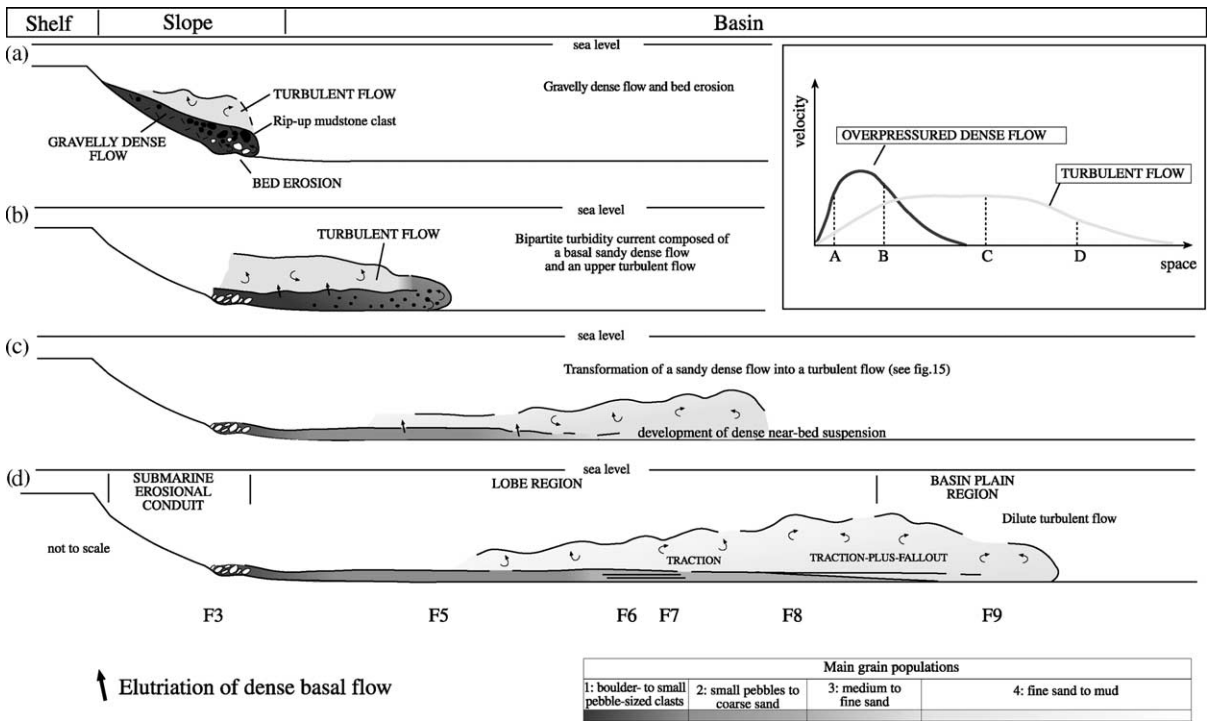

Fig. 4. Main depositional processes acting in a turbidite system dominated by highly efficient bipartite flow (from Mutti et al. (2003)).

sandy dense flow characterised by horizontal grain-size gradient (Fig. 4b).

The basal sandy dense overpressured flow will tend to be progressively depleted of finer particles with time. Within the body, this phenomenon is due to the upward movement of the interstitial water driven by excess pore pressure (elutriation transformation), while at flow margins, due to flow transformation, finer particles will be incorporated into the overlying turbulent flow. As a result, pore fluid pressure within the basal flow will be suppressed and the flow forced to come to rest, depositing massive and crudely graded F5 facies (Fig. 4c).

The development of a genetically related turbulent flow mainly depends on the capability of the dense flow margins to transform, which is principally a function of the coherency (*sensu* Marr et al., 2001; see also Mohrig and Marr (2003)). The overlying turbulent flow thickens downcurrent due to the mixing with ambient fluid and the continuous supply of sediment due to elutriation processes, transformation of flow margins and frontal erosion; when the basal dense flow comes to rest the turbulent flow can outdistance the F5 deposit and carry its suspended load farther basinward to form well sorted laminated F9 facies (Fig. 4d).

Between the deposits related to the basal dense flow (F2, F3, F5) and those related to the turbulent flow (F9), a series of transitional crudely laminated to massive sandy facies occur. They are composed of grain-size populations B and C and are named F6, F7 and F8 (Fig. 4c and d). All things being equal, their deposition is thought to be related to the degree of turbulent energy developed at the leading edge of the basal dense flow during its downcurrent transformation into a turbulent flow. The degree of turbulent energy may be related, among other things, to the rate of deceleration and mixing with ambient fluid. As outlined by Mutti et al. (2003) this transformation process, in the case of slow deceleration and relatively limited mixing, can give rise to a relatively dense near-bed suspension, mainly involving medium and coarse-grained sand where the characteristic particle support mechanisms of both dense and turbulent flows can coexist. This is in agreement with the laboratory experiment results by Mohrig and Marr (2003). The authors observe that the affiliated turbulent flow derived by the transformation of the moderately coherent debris flow front is unable to sustain grain sizes larger than very-fine sand that, in turn, can rapidly settle out onto the top of the basal dense flow. This phenomenon can generate a near bed high density zone in which the high sediment concentrations (Allen & Leeder, 1980), the rate of fallout (Arnott & Hand, 1989) and the mud content (Baas & Best, 2002; Lowe & Guy, 2000) can play a major role in suppressing the turbulence.

After the deposition of F5, the near bed suspension, whose bypass can be enhanced also by traction of the overlying fully turbulent flow, can deposit the F7 and F8 facies. This interpretation is supported by the facies analysis results carried out on the succession present in this paper. The Broto C bed and many other beds outcropping in the Aragues del Puerto section (Figs. 2 and 9) show an F8 facies (that corresponds to the Ta Bouma sequence and is usually described as graded or massive) characterised by crude, cm-thick horizontal laminae, as though there were a continuum with the upcurrent F7 facies (Figs. 3 and 4). This feature is

here interpreted to be related to a dense flow unable to transform into a turbulent flow which would be capable of sustaining a sand fraction coarser than fine; therefore, it would be progressively more concentrated at the base of the flow during its downcurrent evolution. In other words, the turbulent flow forming from the dense flow and bypassing the F5 deposits is characterised by a progressive reconcentration (or gravity transformation) of the coarser grain-size populations, to form a near-bed suspension in which the turbulence tends to be suppressed (Kneller & Branney, 1995; Lowe & Guy, 2000). Such a flow can be seen as a waning, highly stratified bipartite turbulent flow, in which the basal part, dominated by a near-bed high-density suspension, can undergoes traction from the upper part of the flow, dominated by fully turbulence (as testified by the crude horizontal laminations present both in the F7 and F8 facies).

In contrast, when the rate of deceleration (and so of mixing) is high, as can be the case of a hydraulic jump, the head transformation can produce a flow expansion characterised by significant dilution and high turbulent energy. In this case many of the grain-size populations are sustained by the turbulent flow and only the coarser particles settle. A fully turbulent flow, characterised by a strong vertical grain-size segregation, will develop and bypass, thus winnowing and reworking the coarser distal part of the F5 deposit producing the characteristic tractional features of the 3D megaripples (F6 facies). Downstream of this point the suspended load of the turbulent flow can reconcentrate forming a near bed suspension that is responsible for the deposition of the F8 facies (Mutti, 1992; see also Kneller and Branney (1995)). In this way, 3D megaripple (F6) and F7 facies may be considered two end members depositing when the dense flow undergoes rapid and gradual deceleration, respectively. In the first case the production of a fully turbulent flow will tend to predominate, whereas, in the second one, a near bed suspension will be developed (for more details the reader is referred to Mutti et al. (2003)).

In conclusion, the evolution and the facies tract of a deep-water sediment gravity flow can be divided in three main phases (Figs. 3 and 4), related to three types of gravity flow, each characterised by the coexistence of one or more particle support mechanisms. The first phase is related to a basal inertial dense flow, responsible for the deposition of coarser grained F2, F3 and F5 facies, the second phase to the coexistence of a dense near bed suspension and a turbulent flow responsible for the deposition of transitional facies F6–F8 and the third phase to a turbulent flow responsible for well-sorted fine grained F9 facies.

Depending mainly on the grain-size populations of the parent flow and on the type of flow transformations occurring during its motion, each bipartite flow will possess a characteristic efficiency. This efficiency, intended as the ability of a flow to carry its sediment load basinward and to segregate its grain populations into distinct facies types with distance, essentially controls the characteristics of the facies and facies tracts (Mutti et al., 1999). All other things being equal, this is essentially a function of the duration of the flow and of its capacity to transform that, in turn, depends on the coherency (in the sense of Marr et al. (2001)).

In summary (Figs. 3 and 4), highly efficient bipartite flows will be able to develop large turbulent portions and, therefore, will show a facies tract dominated by laminated facies (F6–F9). In contrast, poorly efficient bipartite flows will mainly deposit poorly sorted massive and crudely graded facies (F2, F3 and F5), related to the basal dense flow.

Note that during this phase of the project, no attempt has been made to simulate flows depositing the F2 and F3 facies, and the F6–F8 facies. This choice was made in order to test the new code for dense flow by simulating relatively simple situations and to check the ability of the turbulent flow code to transport various grain-size populations.

3.2. The processes of fluidisation and hindered settling in the basal dense flow: the F5 deposit

F5 facies are extremely common in ancient turbidite systems and because of their lateral extent (up to tens of kilometres, according to Mutti et al. (1999)) and textural properties, they may represent very large volume and high quality reservoirs. Modelling the F5 facies has therefore been considered a key element of this research. This section contains the sedimentologic description of the basic properties of dense overpressured flows on which the dense flow physical model has been built (Section 4).

The origin of this type of facies has been intensely debated over the last few years (see discussion in Shanmugam (2000)). However, theoretical, experimental and field observations tend to confirm that the large lateral extent of relatively coarse grained beds composed by grain sizes characterised by high fall velocities, can only be explained invoking an overpressured dense flow within which the contribution of intergranular friction to momentum dissipation is minimized (Mutti et al., 1999; Norem et al., 1990; see also Major and Iverson (1999)).

As described in Section 3.1, F5 deposition is finally caused by fluidisation processes. Fluidisation, refers to the transformation of a locked granular bed into a fluid-like state. This process, which has been investigated by engineers (Kunii & Levenspiel, 1977, with references), sedimentologists and volcanologists (Allen, 1982; Freundt & Bursik, 1998; Lowe, 1976; Sparks, 1976; Wilson, 1984; with references), is due to the drag exerted on the particles by the upward movement of the interstitial fluid: when the drag balances the weight of the particles, the rigid granular framework breaks down and the bed behaves as a fluid.

In Fig. 5, the minimum fluidisation velocity (V_{mf}) and the fall velocity (V_f) are plotted as a function of the grain-size populations. V_{mf} is defined as the water escape velocity (V_w) at which fluidisation occurs; V_w mainly depends on

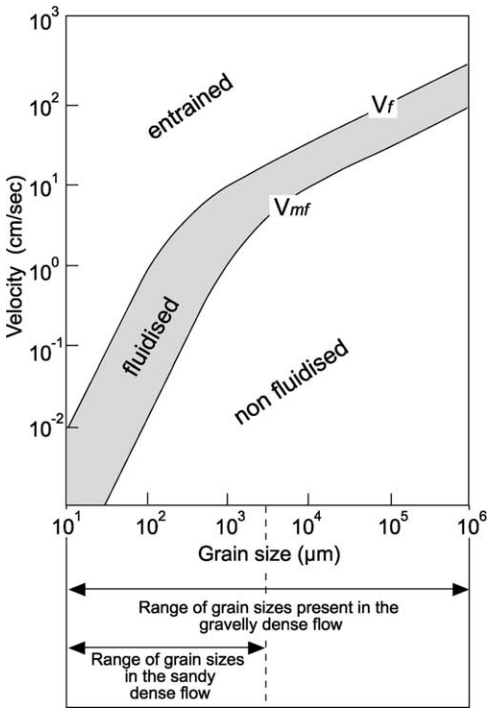

Fig. 5. Water escape velocity versus grain-size diagram showing curves for fall velocity (V_f) and minimum fluidisation velocity (V_{mf}), (slightly modified after Lowe (1976)).

the grain-size distribution that, in turn, controls the permeability.

Fig. 5 shows that in a poorly sorted granular layer, different grain sizes are fluidised under different conditions. For a given V_w, only a fraction of the grain-size population can be fluidised; finer fractions will be fully entrained by the escaping interstitial water and elutriated from the flow. By contrast, the coarser non-fluidised particles will settle according to their buoyancy.

If within the basal dense flow $V_w > V_f$, the elutriation processes will progressively tend to deplete the body of fines, forcing the dense flow to come to rest. The resulting deposit shows a typical vertical grain-size segregation as commonly found in many F5 layers.

Following Iverson (1997) the capacity of a dense flow to produce overpressure is proportional to the Darcy number (N_{dar})

$$N_{dar} = \frac{\mu}{Vl_s \rho_s \gamma k}, \quad (1)$$

where μ is the fluid phase viscosity; Vl_s and ρ_s, the volume fraction and density of the granular phase, respectively; γ, the shear strain rate (du/dy); k is the permeability.

High values of the Darcy number indicate dense flows characterised by a fluid phase rich of fines (silt and clay), that determines a high viscosity and a low permeability of the flow. In this case, for a given shear strain rate, or internal gradient of velocity (du/dy), the developed transient pore-pressure disequilibrium will not dissipate rapidly, producing a significant pore-fluid pressure that can last with time. In contrast, for low values of N_{dar}, a relatively high flow permeability, associated with a relatively low viscosity for the fluid phase results in the rapid dissipation of the excess pore pressure that may have developed.

All other things being equal, the physical conditions generating a high pore-fluid pressure are principally determined by the internal gradient of velocity (du/dy) and by the fines content that control permeability and viscosity. The viscosity of the fluid phase is also important because it can drive the way in which the interstitial water can escape upward (Allen, 1982; Wilson, 1984). In fact, for high values of the fluid phase viscosity (i.e. for high content of fines) and low values of the density contrast between the fluid and the granular phases ($\Delta\rho = \rho_s/\rho_f$), the system tends to develop a *particulate fluidisation* where the interstitial water, escaping upward in a uniform way, can homogeneously redistribute the finer particles in the upper part of the flow. If the flow is characterised by very high content in coarse sediment, an infiltration layer (in the sense of Nichols, Sparks, and Wilson (1994)) may possibly form. This zone will be therefore affected by further reduction of permeability and hence of the time of diffusion of the overpressure. In contrast, when the fluid viscosity is low (i.e. low content of fines) and so the density ratio ($\Delta\rho = \rho_s/\rho_f$) is high, the system shows an *aggregative fluidisation*, in which the interstitial water, concentrating in channels and pillars, can escape more rapidly and dissipate quickly the excess pore-fluid pressure.

Moreover, fluidisation implies that a continuous source of water is available throughout motion of the dense flow. The two most plausible processes that can be invoked to explain the occurrence of a continuous water supply to the system are: (1) injection of water at the base of the frontal part of the flow related to hydroplaning phenomena (Mohrig et al., 1998) and (2) self-fluidisation related to hindered settling of concentrated dispersion (Freundt & Bursik, 1998). If the first process is more likely to be associated with any transformation of the leading edge of the dense flow, the second one seems to better explain the overpressure conditions in the body of the flow. Experiments on the settling behaviour of poorly sorted, high-concentration granular dispersions have, in fact, produced segregation structures very similar to those obtained in fluidisation runs (Druitt, 1995). Hindered settling and fluidisation processes can therefore be considered hydrodynamically very similar and so they may generate similar segregation structures. The main difference is that in hindered settling, particles move downward and displace the fluid, whereas in the fluidisation runs the fluid source is imposed externally, but in both cases there is a relative vertical motion between grains and fluid. In this way, hindered settling of concentrated, poorly sorted dispersions can be considered a type of self-fluidisation in which the sedimentation of coarser particles causes a sufficiently strong vertical fluid flux able to fluidise and

possibly elutriate the finer ones (Druitt, 1995; Freundt & Bursik, 1998).

At least two variables (in addition to shear strain rate and viscosity of fluid phase) have to be considered as controlling factors for the generation of overpressure in dense flows: (1) the presence and the amount of coarse grain-size populations (cf. Hampton, 1979) and (2) the thickness of the flow, which sets the pressure that can be transferred from the granular phase to the fluid phase (see the discussion related to Fig. 15 in Section 5).

4. Physical model

The model presented in this paper is a first attempt to describe the evolution of the basal dense flow and of the generation and evolution of the associated turbulent flow. This is done by coupling two different models, one for the basal dense flow and the other for the overlying turbulent flow.

The model has to be considered only a first step in the description of a real event, as some features of a natural flow are not included. Nevertheless, the merit of the model lies both in its capacity to be used to interpret and describe a large range of phenomena occurring during a real event and, by comparison to experimental and field observations, in its utility to highlight what is poorly understood physically and requires further study.

A specific description of the model capability or deficiency is reported in Section 6.

4.1. Dense flow model

A depth-averaged one-dimensional model has been developed to describe the motion of fluidised mass flows. A scheme of a fluidised sediment flow is shown in Fig. 6.

A description for the excess pore-fluid pressure and for the effect of upward pore-fluid flow are among the main features of the model, as they determine the degree of fluidisation and the distribution of the particle sizes within the flowing mass.

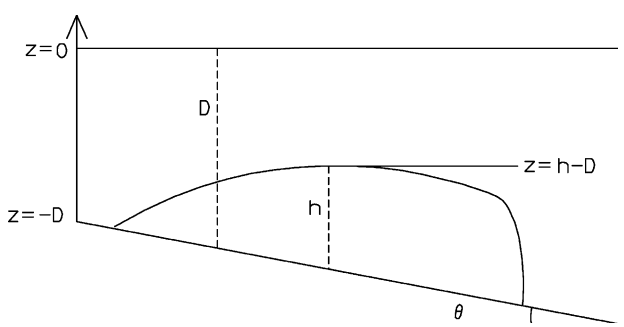

Fig. 6. Diagram illustrating the fluidised sediment flow variables. The vertical co-ordinate z is positive upward and equal to zero at the mean free surface level (D: water depth, h: flow thickness, θ : bottom slope).

Following Iverson and Denlinger (2001) the excess pore pressure is assumed to vary linearly with flow depth

$$P_e = \rho g \lambda (h - D - z), \qquad P_e|_{z=-D} = \rho g h \lambda = P_{BED}, \tag{2}$$

where ρ is the solid/water mixture density; D, the water depth; h, the flow thickness; $0 \leq \lambda < 1$ defines the amount of excess pore pressure as a fraction of the hydrostatic pressure. In the model, according to Iverson and Denlinger (2001), the equation that rules the time rate of change of the basal excess pore pressure P_{BED}, and consequently the vertical profile of P_e is

$$\frac{\partial P_{BED}}{\partial t} + \bar{u}\frac{\partial P_{BED}}{\partial x} = D_H \left.\frac{\partial^2 P_e}{\partial z^2}\right|_{z=-D}, \tag{3}$$

where $\bar{u}$ is the depth-averaged horizontal velocity and D_H is the pore pressure hydraulic diffusivity of the sediment mixture. As advection and diffusion operate on different time-scales, they can be solved sequentially, calculating firstly the advective changes and then correcting the values of P_{BED} with the diffusive contribution given by the linear differential equation

$$\frac{\partial P_{BED}}{\partial t} = D_H \left.\frac{\partial^2 P_e}{\partial z^2}\right|_{z=-D}. \tag{4}$$

This equation is solved by applying the following boundary conditions

$$P_e(z,0) = \rho g \lambda_0 (h - D - z), \qquad \frac{\partial P_e}{\partial z}(-D,t) = 0, \qquad P_e(h - D, t) = 0, \tag{5}$$

where λ_0 establishes the initial amount of excess pore pressure. A resulting solution describing P_{BED} is given in Iverson and Denlinger (2001) and derived by Carslaw and Jaeger (1959):

$$\begin{aligned} P_{BED}(-D,t) &= \rho g h \lambda \\ &= \rho g h \lambda_0 \left\{ 1 - 2 \sum_{n=0}^{\infty} \left[(-1)^n \operatorname{erfc}\left((2n+1)\frac{h}{\sqrt{4 D_H t}} \right) \right] \right\}. \end{aligned} \tag{6}$$

In the present model, a water replenishment from the flow base is assumed, partially accounting for the water loss at the upper boundary, due to the upper flux generated by the excess pore pressure. As previously noted in Section 3.2, the water replenishment is considered one of the main mechanisms for maintaining an excess pore pressure for long time and distances.

Presently, the mechanisms and phenomena governing the water replenishment is considered to be too uncertain for a complete modelling of the water balance, therefore, this issue has been parameterised by the hydraulic diffusivity

D_H. A reduction of the D_H parameter causes a reduction of the amount of escaping water. This accounts for the partial water replenishment from the base of the flow.

Consequently, the hydraulic diffusivity parameter D_H should be considered a model calibration parameter, that has been determined according to the observed distances covered by the overpressured flow.

As previously observed, the excess pore pressure causes an escape velocity of the fluid V_w that supports the sediment. V_w is calculated by the Darcy law

$$V_w = -\frac{k}{\mu_f}\frac{\partial P_e}{\partial z} = \frac{k}{\mu_f}\rho g\lambda, \tag{7}$$

where k is the permeability and μ_f is the fluid viscosity. The permeability k is calculated by the empirical formula (Fair & Hatch, 1933)

$$k = \frac{1}{A\left[\frac{(1-n)^2}{n^3}\left(B\sum_i \frac{c_i}{100 d_{50}}\right)^2\right]}, \tag{8}$$

where n is the porosity; c_i, the sediment concentration; d_{50} represents the grain size, $A \approx 5$ and $6 \leq B \leq 7.7$.

The effect of the upward flux V_w is introduced following Lowe (1976), Sparks (1976) and Wilson (1984). They proposed that fluidised flows are actually only partly fluidised and three different conditions coexist causing three different behaviours:

(a) particles with fall velocity V_f lower than V_w : $V_f < V_w$;
(b) particles with fall velocity V_f larger than V_w and minimum fluidisation velocity V_{mf} lower than V_w : $V_f \geq V_w \geq V_{mf}$;
(c) particles with minimum fluidisation velocity V_{mf} larger than V_w : $V_{mf} > V_w$.

Values for particle fall velocity V_f and minimum fluidisation velocity V_{mf} adopted in the model are shown in Fig. 5.

Type (a) particles are transported by the upward flux and tend to be lost by elutriation and to form the turbulent cloud of sediment above the fluidised flow. Type (b) particles form the matrix of the fluidised flow and their weight is balanced by the upward flux. Type (c) particles tend to sink into the matrix and deposit at the bottom of the flow. Applied in the present model, this produces a selective sorting of the different grain sizes that tends to transport upward the finer classes of sediment, for which $V_w > V_{f,i}$, and downward the coarser classes, for which $V_w < V_{mf,i}$ (where i indicates each grain-size population).

At the upper boundary, the finer classes of sediment are elutriated, and pass into the turbulent flow, at the lower boundary, deposition of the coarser classes occurs.

It should be noted that this vertical grain-size sorting causes an increase of the finer classes concentration in the upper part of the flow. This produces a decrease of the permeability k and consequently of the water escape velocity V_w, which contributes to maintain the overpressure (cf. Section 3.2).

The present model uses a certain number of sediment grain-size populations and a certain number of layers inside the fluidised sediment mass in order to provide a description of the vertical sorting of the different classes of sediment that occurs during the flow.

Fig. 7 shows a scheme of this mechanism. In this example, four sediment size classes and four layers inside the flowing mass are considered. The finest grain-size population is transported upward and is elutriated, the coarsest sinks and is deposited, while the remaining intermediate classes form the matrix.

The differential equations describing the motion of the flow are presented below.

The depth-averaged mass conservation equation is

$$\frac{\partial h}{\partial t} + \frac{\partial(h\bar{u})}{\partial x} = \text{flux}|_{z=-D} - \text{flux}|_{z=h-D}, \tag{9}$$

where *flux* is the water/sediment flux at the upper boundary due to fine sediment elutriation and represents the sediment flux at the lower boundary due to sediment deposition (*flux* is positive upward).

The conservation equations of sediment concentration for each grain-size fraction and for each layer are expressed by

$$\frac{\partial(\tilde{h}c_i)}{\partial t} + \frac{\partial(\tilde{h}\bar{u}c_i)}{\partial x} = \text{flux}_i|_0 - \text{flux}_i|_{\tilde{h}}, \tag{10}$$

where $\tilde{h}$ is the height of each layer, $\text{flux}_i|_0$ and $\text{flux}_i|_{\tilde{h}}$ are the fluxes of the respective grain-size population at the lower and upper boundaries of the layer. The fluxes are calculated by

$$\text{flux}_i = c_i(V_w - V_{r,i})\text{fact}, \tag{11}$$

where $V_{r,i}$ can be alternatively the sediment falling velocity $V_{f,i}$ if $V_w > V_{f,i}$, the minimum fluidisation velocity $V_{mf,i}$ if $V_w < V_{mf,i}$ or the escape velocity of fluid itself V_w if $V_{mf,i} \leq V_w \leq V_{f,i}$.

The boundary conditions at the lower and upper boundary of the flow are given by the fluxes $\text{flux}_i|_{z=-D}$ and $\text{flux}_i|_{z=h-D}$ that represent, respectively, the volume of

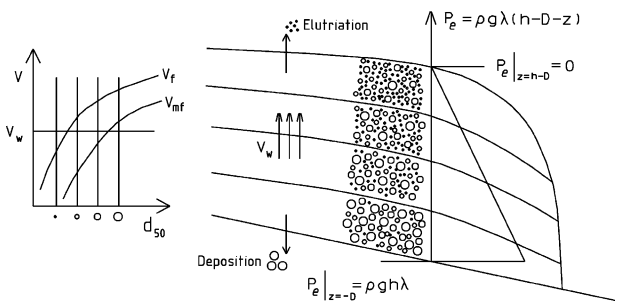

Fig. 7. Scheme of the fluidisation framework (see text for variable definitions).

sediment for each grain-size population that is deposited or elutriated.

Fact represents a reduction factor of the displacement velocity for sediment grains in high concentration water–sediment mixtures with respect to clear water. It is experimentally derived by Richardson and Zaki (1954) for sediment grain size ranging between 50 and 500 μm and is given by

$$\text{fact} = (1 - c_T)^{\gamma}, \qquad \gamma \approx 4, \tag{12}$$

where c_T is the total sediment concentration.

The equation of momentum conservation is derived assuming the following stress components

$$\tau_{zx} = \tau_{\text{yield}} + \mu_B \frac{\partial u}{\partial z}, \tag{13}$$

where μ_B is the bulk viscosity of the flux and

$$\tau_{\text{yield}} = (\sigma - P_e)\tan\varphi, \tag{14}$$

where σ is the total compressive normal stress; $\sigma - P_e$, the intergranular effective stress; φ is the internal friction angle

$$\tau_{xx} = \mu_B \frac{\partial u}{\partial x}. \tag{15}$$

The resulting depth-averaged horizontal momentum conservation equation is

$$\frac{\partial(h\bar{u})}{\partial t} + \frac{\partial(h\bar{u}^2)}{\partial x} = -\left[\frac{\rho_f - \rho_w}{\rho_f} gh\frac{\partial(h-D)}{\partial x} + gh\lambda\frac{\partial(h-D)}{\partial x} + \frac{1}{2}gh^2\frac{\partial\lambda}{\partial x}\right] - gh(1-\lambda)\text{sgn}(\bar{u})\tan\varphi_{\text{bed}} + \frac{\mu_B}{\rho_f}h\frac{\partial^2\bar{u}}{\partial x^2} - 3\frac{\mu_B}{\rho_f}\frac{\bar{u}}{h}, \tag{16}$$

where ρ_f is the density of the flowing mass; ρ_w, the density of the surrounding water; φ_{bed}, the bed friction angle; μ_B is the bulk viscosity. The terms on the right hand side of Eq. (16) represent the depth-averaged horizontal pressure gradient, the frictional locking occurring at the bottom of the mass and the depth averaged horizontal diffusion component and vertical diffusion component, respectively. The form of the vertical diffusion component derives from the assumption of laminar flow and, therefore, of a parabolic vertical profile of velocity inside the flowing mass.

Assuming that both the horizontal velocity gradient at the dense flow/ambient water interface and the velocity at the bottom of the flow are equal to zero, the resulting vertical profile of velocity is

$$u(z) = \frac{3}{2}\frac{\bar{u}}{h^2}[D(2h-D) + 2z(h-D) - z^2]. \tag{17}$$

Assuming that the velocity profile of the upper part of the flow is constant, when τ_{zx} is lower than τ_y, the parabolic profile in Eq. (13) is considered as an approximation of the real vertical profile. Nevertheless, in our opinion the parabolic profile is a reasonable assumption for the following reasons: (a) the parabolic profile is the correct profile or a very good approximation of the parabolic/constant profile when a large excess pore pressure is present in the flow, and (b) the use of the real parabolic/constant profile would result only in a different coefficient of vertical diffusion component (Iverson & Denlinger, 2001).

The form of the depth-averaged horizontal pressure gradient is obtained assuming the following vertical pressure profile inside the flowing mass ($-D \le z \le h - D$), where the contribution of the sea surface elevation has been neglected:

$$P_T(z) = \int_{h-D}^{0} \rho_w g\,dz + \int_{z}^{h-D} \rho_f g(1+\lambda)dz = -\rho_w g(h-D) + \rho_f g(1+\lambda)(h-D-z). \tag{18}$$

The depth-averaged horizontal gradient of this pressure profile gives

$$-\frac{1}{h}\int_{-D}^{h-D}\frac{\partial P_T}{\partial x}dz = -(\rho_f - \rho_w)g\frac{\partial(h-D)}{\partial x} - \rho_f g\lambda\frac{\partial(h-D)}{\partial x} - \frac{h}{2}\rho_f g\frac{\partial\lambda}{\partial x}, \tag{19}$$

from which the term in Eq. (16) is easily derivable.

A complex phenomenon that is neglected in the model is the transformation of the head of the flow. It is difficult to state the relevance of this deficiency; some consideration will be made in the discussion of the results to field data comparison and in the conclusions.

A finite difference technique is adopted for the numerical integration of the equations. The spatial discretisation of the governing equations is carried out on a staggered grid, where the scalar quantities, namely the mass height h, the excess pore pressure at the bed P_{BED} and the fractions of sediment grain-size populations c_i, $i = 1, n$, are evaluated in the middle of each mesh, while averaged velocity $\bar{u}$ is evaluated at the right hand side of each cell. Time discretisation is carried out using a staggered time step where scalar quantities and velocity are computed at half time step distance. A first order upwind scheme is used for the integration of the advection term.

At the flow front an algorithm is applied to avoid spurious diffusion and flattening of the front slope. The exact front position inside the front cell is computed by moving the front with the speed computed at the adjacent cell. The height of the flowing mass in the front cell is computed by a mass flux balance.

4.2. Turbulent flow model

The turbulent flow model has been described in Drago (2002) and Drago and Terenzi (2001). It is a 2D hydrodynamic model with variable density depending

on the sediment concentration and a $K-l$ turbulence closure model based on the Mellor and Yamada (1982) formulation. Hereafter, only the coupling of the dense flow/turbulent flow models (i.e. the bottom boundary conditions of the turbulent flow model) is described; for a complete description of the turbulent flow model, the reader is referred to Drago (2002). Drago (2002) also describes the coupling of the turbulent flow model with a debris flow model based on a Bingham rheology (Jiang & Le Blond, 1993; Liu & Mei, 1989) in order to simulate the generation of a turbulent flow due to the occurrence of a debris flow.

The coupling with the dense flow model is similar to that adopted for the coupling to the previously mentioned debris flow model, but with some different features. The coupling is obtained by imposing, at the bottom boundary of the turbulent flow model, the velocity of the upper boundary of the dense flow model and by including a source term for sediment flux equal to the sediment that is elutriated from the fluidised sediment mass during flow. Sediment erosion from the top of the fluidised sediment mass due to the shear stress exerted by the turbulent flow is also considered.

The velocity for the upper boundary of the dense flow model is obtained from the mean velocity by the relation $U_{up} = (3/2)\bar{u}$ assuming a parabolic vertical profile of velocity (Eq. (17)).

This velocity generates a shear stress that starts to develop, for the overlying turbulent flow, a vertical profile of current velocity, sediment concentration and turbulent kinetic energy. The bottom shear stress is equal to

$$\tau_b = u_*^2 \rho, \tag{20}$$

where ρ is density and u_* is the friction velocity obtained assuming a logarithmic profile of longitudinal velocity at the turbulent flow/dense flow boundary or at the turbulent flow/sea bed interface, and that is expressed by the wall function of Rodi (1980)

$$u_* = \frac{(u(z) - U_{up})k_n}{\ln[(z + z_0)/z_0]}, \tag{21}$$

where $u(z)$ is the horizontal velocity at a distance z from the sea bed; z_0 represents the sea bed roughness (Van Rijn, 1989); k_n, the Von Karman constant; U_{up} is the velocity of the upper boundary of the associated dense flow for the duration and extension of the flow itself and is equal to zero elsewhere in time and space. The boundary condition for the horizontal component of current speed $u(z)$ is obtained imposing at the bottom

$$\nu_t \left.\frac{\partial u}{\partial z}\right|_{z=0} = \tau_b = u_*^2 \rho, \tag{22}$$

where ν_t is the eddy viscosity.

The source of each of the n classes of suspended sediment at the sea bottom is given by

$$\text{source}_i = E_i(\tau_b - \tau_{cr})F_i + \text{flux}_i|_{z=h-D}, \qquad i = 1, n, \tag{23}$$

where E_i is the ith sediment grain-size population entrainment coefficient, τ_{cr} is the critical stress for initiation of sediment erosion determined by the Shield relation (Van Rijn, 1989), F_i is the fraction of sediment grain-size population at the upper boundary of the dense flow and $\text{flux}_i|_{z=h-D}$ is the flux of the ith grain-size population elutriated by the fluidised sediment mass.

Another important new feature of the present model is that the entire water column, including the free surface elevation variation, is considered. This is done including into the model a surface layer extending from the top of the 2D model domain to the free surface. The resulting computational domain is depicted in Fig. 8.

For the surface layer, depth-averaged equations are implemented: the continuity equation

$$\frac{\partial \eta}{\partial t} + \frac{\partial[(Q + \eta)\bar{U}]}{\partial x} - \tilde{V} = 0. \tag{24}$$

The momentum conservation equation is

$$\frac{\partial \bar{U}}{\partial t} + \bar{U}\frac{\partial \bar{U}}{\partial x} + \frac{1}{\rho}\frac{\partial P}{\partial x} = -SgC_T \sin\theta + \frac{\partial}{\partial x}\left(\nu_t \frac{\partial \bar{U}}{\partial x}\right), \tag{25}$$

where P is pressure; S, the submerged specific gravity of the sediment (≈ 1.65), C_T, the total sediment concentration; ν_t is the eddy viscosity.

Including the variation of the free surface from the mean sea level, and considering that

$$\rho = \rho_w(1 + SC_T), \tag{26}$$

where ρ_w is the water density, the vertical profile of pressure is given by

$$P(z) = \rho_w g(\eta - z) + \rho_w \int_z^\eta SC_T g \, dz. \tag{27}$$

It is evident that into the horizontal-pressure gradient, beside the contribution due to the density variation induced

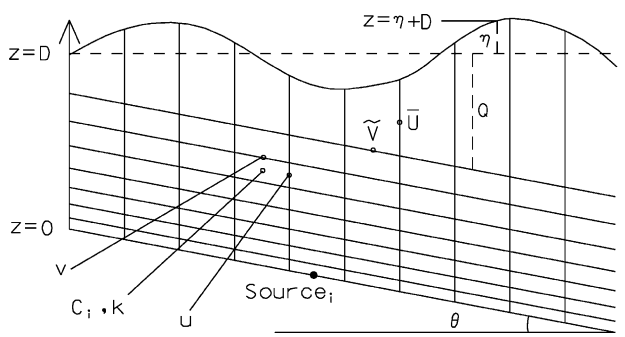

Fig. 8. Scheme of the turbulent flow model computational domain with variables and their calculation position. The vertical co-ordinate z is positive upward and equal to zero at the sea bottom. (D: water depth, η: free surface elevation, v: vertical component of velocity, u: horizontal component of velocity, C_i: suspended sediment concentration of the ith grain-size class, k: turbulent kinetic energy, $\tilde{V}$: vertical velocity component at the uppermost regular grid mesh, $\bar{U}$: mean horizontal velocity in the surface layer, Q: thickness of the surface layer, θ: bottom slope).

by the sediment concentration, a contribution due to the free surface slope is introduced.

5. Numerical modelling: description of the results

As indicated in Section 2, the modelling presented here focuses on a single bed from the Broto turbidite system (Eocene of the south central Pyrenees) and is referred to here as, Broto C. The bed has been described in detail at four different locations and, because of its facies tract, it is interpreted as having been deposited by a highly efficient, subaqueous, bipartite gravity flow (Fig. 9, cf. Section 3). Fig. 9 shows the simplified genetic facies tract of the Broto C bed. For every measured field section, a detailed facies interpretation and the sample location are also indicated. With respect to the ideal facies tract shown in Fig. 3, this bed does not show the 3D megaripples typical of facies F6, indicating that, as explained in Section 3, the transitional evolutionary phase of the flow is dominated by near-bed suspension, rather than by high-energy turbulence.

The simulation has been performed through three main steps: (1) estimation of the parent flow volume and grain-size populations; (2) choosing of the initial flow conditions, external ambient conditions (sea bottom gradient) and physical parameters governing the flow and (3) execution of the coupled numerical models and comparison of the results with the field data (the codes simulating dense and turbulent flows have been informally named DENS_FLOW and TURB_FLOW, respectively).

Step 1. For each facies type, the bulk volume has been calculated by estimating the related areas on the cross-section of Fig. 9; the total solid volume is obtained by summing the volumes for the individual facies, assuming an average present-day porosity of 20%.

According to the field observations and the grain-size analysis results, seven grain-size populations, ranging from clay to very-coarse sand, have been considered. For each facies, the characteristic grain-size populations have been calculated by averaging the grain-size distribution of the samples belonging to that facies. The grain-size populations of the entire bed are computed averaging the grain-size distribution of the individual facies, weighted with the individual facies solid volume. Both the total solid volume and grain-size populations are assumed to be representative of the parent flow.

Table 1 summarises the resulting bulk volumes and grain-size populations. Note that the uppermost, shaly part

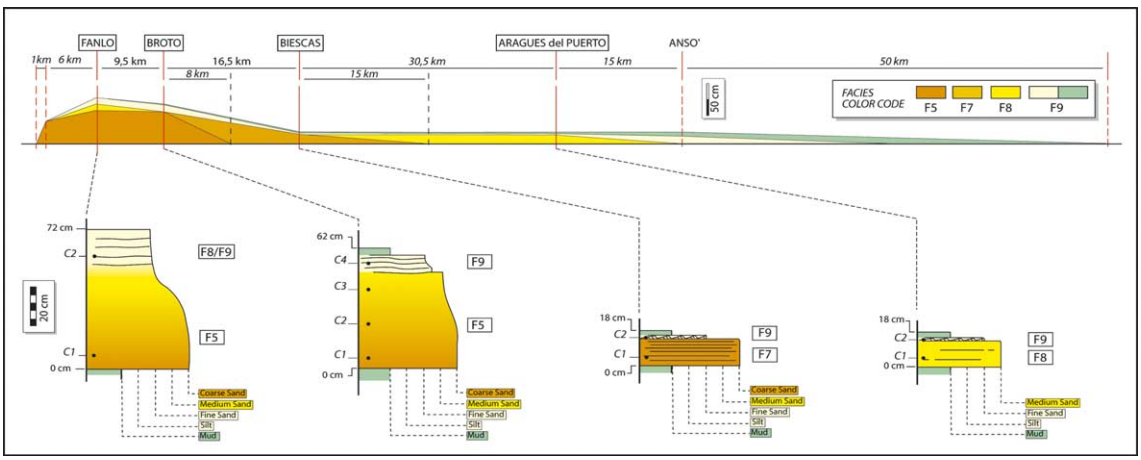

Fig. 9. Simplified physical reconstruction of the genetic facies tract for the Broto C bed (see Fig. 2 for location). For each measured section the location of the samples collected for grain-size analysis are indicated. Beyond the measured sections (Fanlo to Aragues del Puerto), distances and bed characteristics have been extrapolated on the basis of the regional geological knowledge (Section 2).

Table 1
Estimation of volume and grain-size populations for each facies

Facies	V_{bulk} (m^3)	Grain-size populations (%)						
		Very coarse sand	Coarse sand	Medium sand	Fine sand	Very fine sand	Silt	Clay
F5	9805	0.0	17.5	29.2	27.7	9.7	4.5	11.4
F7	4285	8.3	39.9	19.4	10.5	6.6	4.3	11.0
F8	4118	0.0	3.4	30.2	33.0	16.8	6.7	10.0
F9	10,358	0.0	4.2	5.0	12.1	13.0	30.1	35.6
Total	28,566	1.3	14.0	19.1	20.2	11.5	10.4	23.6

of the F9 deposits, has been assumed to have silt/clay ratio equal to 1. This approximation is due to the lack, in the measured sections, of significant amounts of F9 mud, which is interpreted to have mainly bypassed the proximal area, and deposited farther basinward. As the bed characteristics have been estimated in this part of the basin (Fig. 9), it seemed reasonable, on the basis of the general geologic setting, to assume such a silt/clay ratio.

Step 2. The flow is considered entering the basin as a continuous overpressured flow. Once the duration of the inflow is selected, the height (h) and the speed ($\bar{u}$) of the flow are assigned by assuming that the flow is in stationary conditions and initially in equilibrium with the slope it is travelling on. Neglecting spatial and temporal derivatives of variables in Eq. (16), it results

$$gh\tan\theta\left[\frac{\rho_f-\rho_w}{\rho_f}+\lambda\right]-gh(1-\lambda)\mathrm{sgn}(\bar{u})\tan\varphi_{bed}=3\frac{\mu_B}{\rho_f}\frac{\bar{u}}{h}. \quad (28)$$

Once the excess pore pressure parameter λ and the bottom slope angle at the inflow point θ are fixed, Eq. (28) provides the relation between the initial values of the height h and the speed $\bar{u}$. A uniform initial vertical distribution of grain-size populations, equal to the composition of the total volume reported in Table 1, has been assumed.

Table 2 shows the input flow conditions and the assigned sea bottom gradient. The latter has been assumed according to the regional geologic knowledge of the basin (Mutti, 1971; Mutti et al., 1985; Mutti et al., 1988; Remacha et al., 1998).

The flow is characterised by physical parameters, most of which are not constrained by field measurements. Therefore, some of these parameters have been varied within a reasonable range of values to better reproduce the geometry and grain-size populations of the deposit. The flow being bipartite, the parameters can be regrouped in two subsets, relative to the dense overpressured and turbulent phases, respectively. Table 3 shows the input parameter sets used for the simulation described below.

The parameter set relative to the dense flow allows to check the capability of the DENS_FLOW code to simulate the fluidisation of the different grain-size populations. Calculating the initial upward flux velocity of the fluid phase and plotting the result in the diagram

Table 2
Flow initial conditions and assumed sea bottom profile

Solid volume	22,853 m^3
Flow porosity	0.5
Flow bulk volume	45,706 m^3
Input flow duration	30 min
Input flow height, h	4.52 m
Input flow velocity, u	5.61 m/s
Sea bottom profile	First 33 km: −2°, next 7 km: −1°, beyond: 0°

Table 3
Physical flow parameters

Dense flow		Turbulent flow	
Flow porosity, n	0.5	Sediment entrainment coefficient, E	5×10^{-7}
Interstitial fluid viscosity, μ_f (Pa s)	0.12	Sea bottom roughness, z_0 (m)	0.1
Flow bulk viscosity, μ_B (Pa s)	200	Turbulence length scale calibration parameter, β[a]	0.30
Flow bulk density, ρ_f (kg/m^3)	2000	Schmidt number, σ[a]	1
Surrounding water density, ρ_w (kg/m^3)	1000		
Bed friction angle, φ_{bed} (°)	35		
Initial excess pore pressure, λ	0.94		
Pore pressure hydraulic diffusivity, D_H (m^2/s)	10^{-5}		

[a] For the definition and possible values, see Drago (2001).

of Fig. 5, together with the V_f and V_{mf} curves, the mechanical behaviour of the different grain-size populations can be determined: it is expected that the modelled dense flow will lose the very-coarse grained sand by sedimentation, will tend to lose the finest populations (very fine sand to clay) by elutriation, whereas will keep the coarse to fine grained particles as fluidised fraction (Table 4).

Step 3. The numerical modelling starts with the run of the DENS_FLOW code, simulating the dense flow, followed by the run of the TURB_FLOW code, simulating the evolution of the turbulent flow.

Fig. 10 shows the whole modelled deposit of both the dense and the turbulent flows (Fig. 10a), compared to the geological reconstruction, represented at the same scale (Fig. 10b). It is observed that the coupled model is able to separate the two types of flow, placing their deposits in the correct order along the depositional profile. Moreover, the model satisfactorily reproduces the F5 and F9 facies both in terms of volumes and travelled distance from the source

Table 4
Mechanical behaviour of the grain-size populations in the overpressured dense flow at initial conditions

Grain size	Mechanical behaviour
Very coarse sand	Sedimentation
Coarse sand	Fluidisation
Medium sand	Fluidisation
Fine sand	Fluidisation
Very fine sand	Elutriation
Silt	Elutriation
Clay	Elutriation

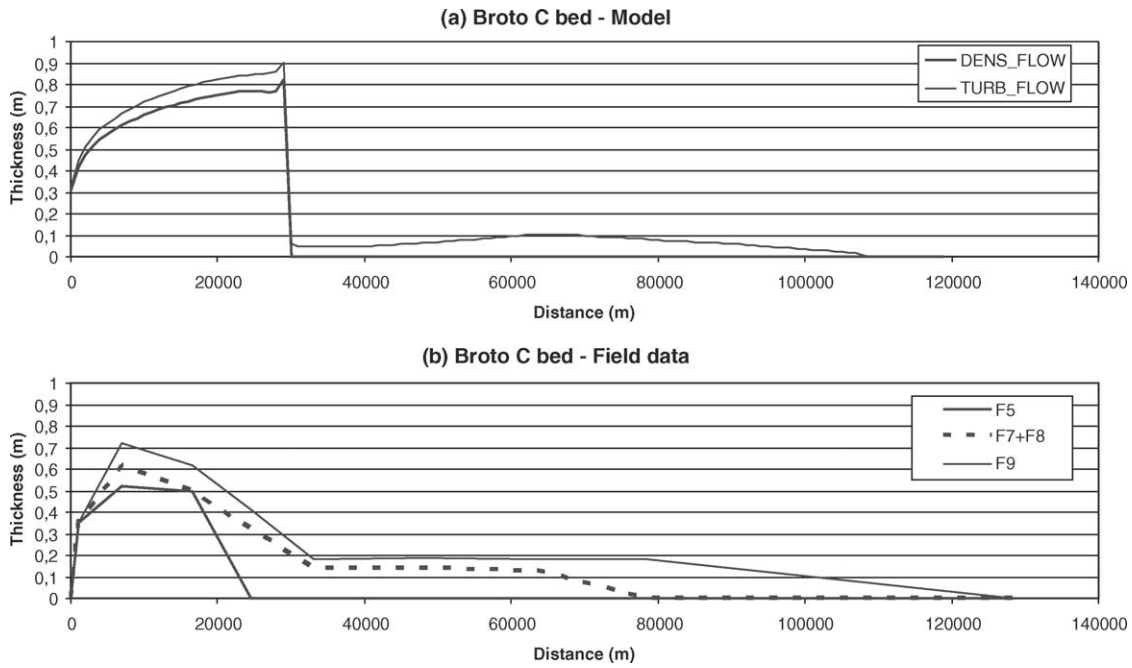

Fig. 10. Bed simulation (a) compared with the geologic reconstruction (b). The modelled profile of TURB_FLOW represents one simulated day of flow evolution and deposition. At this time the only grain sizes still present in suspension are clays and minor silts.

area, but fails to reproduce the F7 and F8 facies (Fig. 11). A brief discussion about this deficiency is given in Section 6.

The peculiarity of both the DENS_FLOW and TURB_-FLOW codes is the ability to provide calculated grain-size distributions directly comparable with the field data (Figs. 12 and 13). In Fig. 12, the grain-size analyses of four samples collected within the F5 deposits (see location in Fig. 9) are compared to the grain-size distributions calculated by the model (DENS_FLOW code) in the equivalent positions. Notice that the absolute error, for each grain size, never exceeds 10%.

In Fig. 13, the same type of comparison is shown for two samples collected within the F9 deposits (see location in Fig. 9). The corresponding grain-size distributions on the model have been calculated by the TURB_FLOW code. Although on average, a worse result has been obtained with

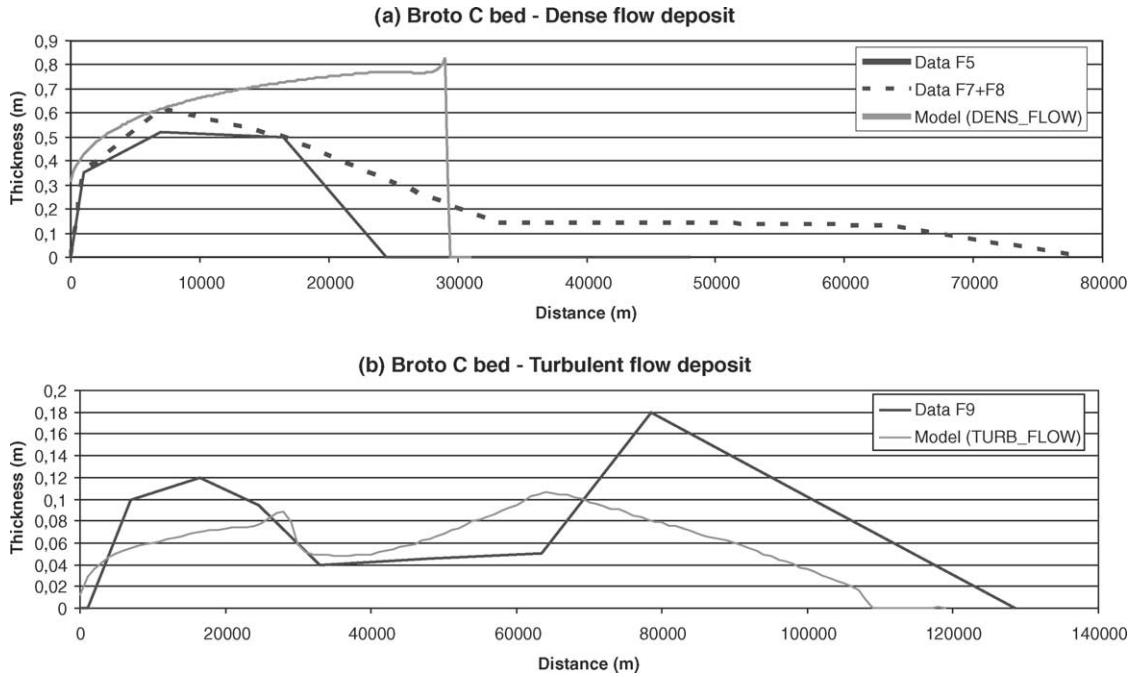

Fig. 11. Comparison between the simulated and real deposit of the coarser facies modelled with the DENSE_FLOW model (a), and of the finer facies modelled with the TURB_FLOW model (b). Coarser facies are F5, F7 and F8, finer facies is F9.

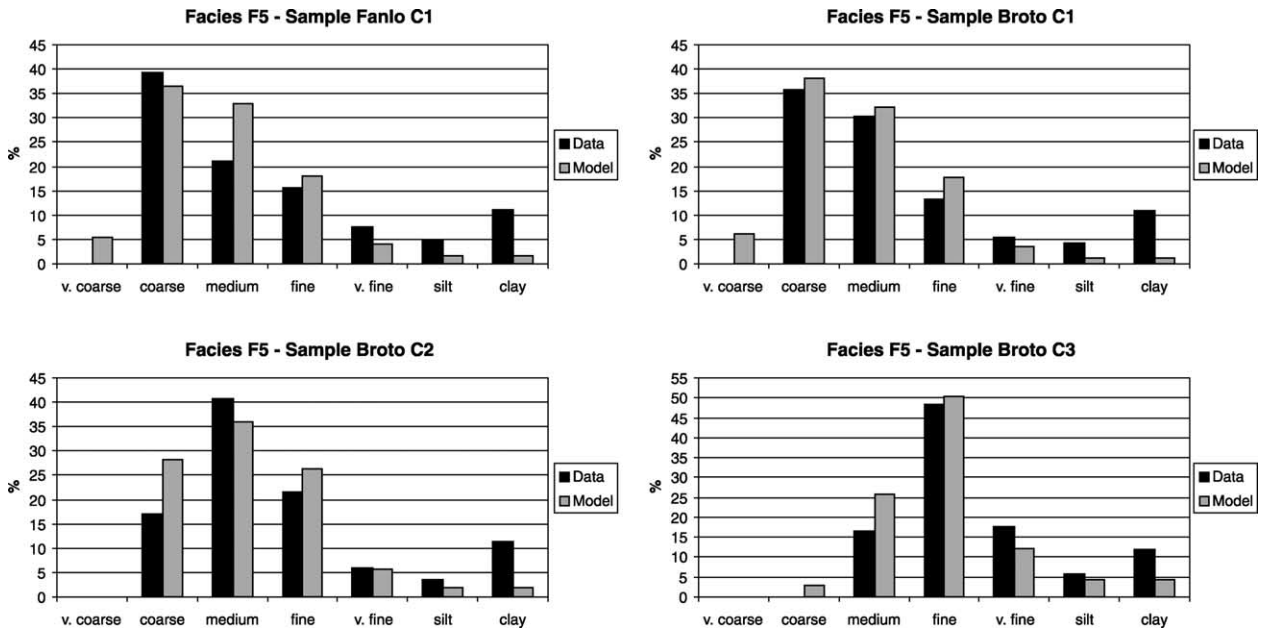

Fig. 12. Comparison between simulated and measured grain-size distributions for samples belonging to coarser-grained facies (F5). See Fig. 9 for sample location.

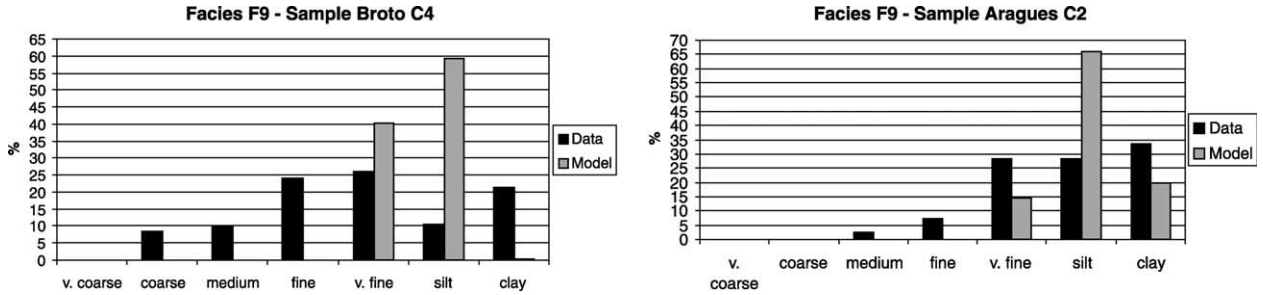

Fig. 13. Comparison between simulated and measured grain-size distributions for facies F9. See Fig. 9 for sample location.

respect to the dense flow deposits, the modelled grain-size populations of the sample Aragues C2 fits relatively well the field data, predicting correctly the main grain-size populations of the sample, but not their absolute values. Conversely, the sample Broto C4 shows an excess, in the field data, of grains coarser than fine sand (that, following the adopted facies classification, cannot be part of the F9 facies). It is supposed that, due to the thinness of the F9 facies in this location (Fig. 9), the collected sample might contain part of the underlying F5 deposit.

Finally, it should be outlined that the DENS_FLOW code is able to simulate the vertical grading typical of many dense flow deposits. In Fig. 14a the grain-size distributions of three samples (C1–C3) are plotted. These are collected, from bottom to top, in the Broto section (Fig. 9), and clearly show the vertical grading of the F5 deposit at this location. In Fig. 14b the corresponding grain size plots obtained from the simulation model are shown; they testify the ability of the DENS_FLOW code to reproduce the same vertical trend.

Another interesting peculiarity of the DENS_FLOW code is well represented in Fig. 15, in which it is shown how

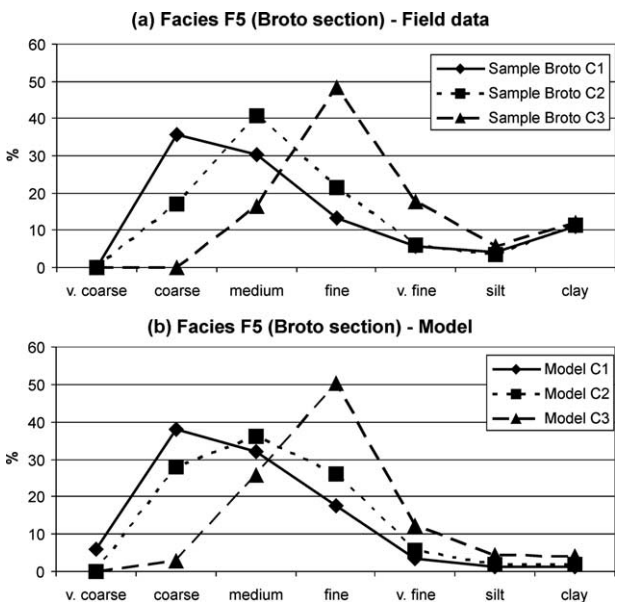

Fig. 14. Comparison between the measured (a) and simulated (b) grain-size distributions for the samples of the facies F5 in the Broto section, showing the vertical grading of the F5 facies.

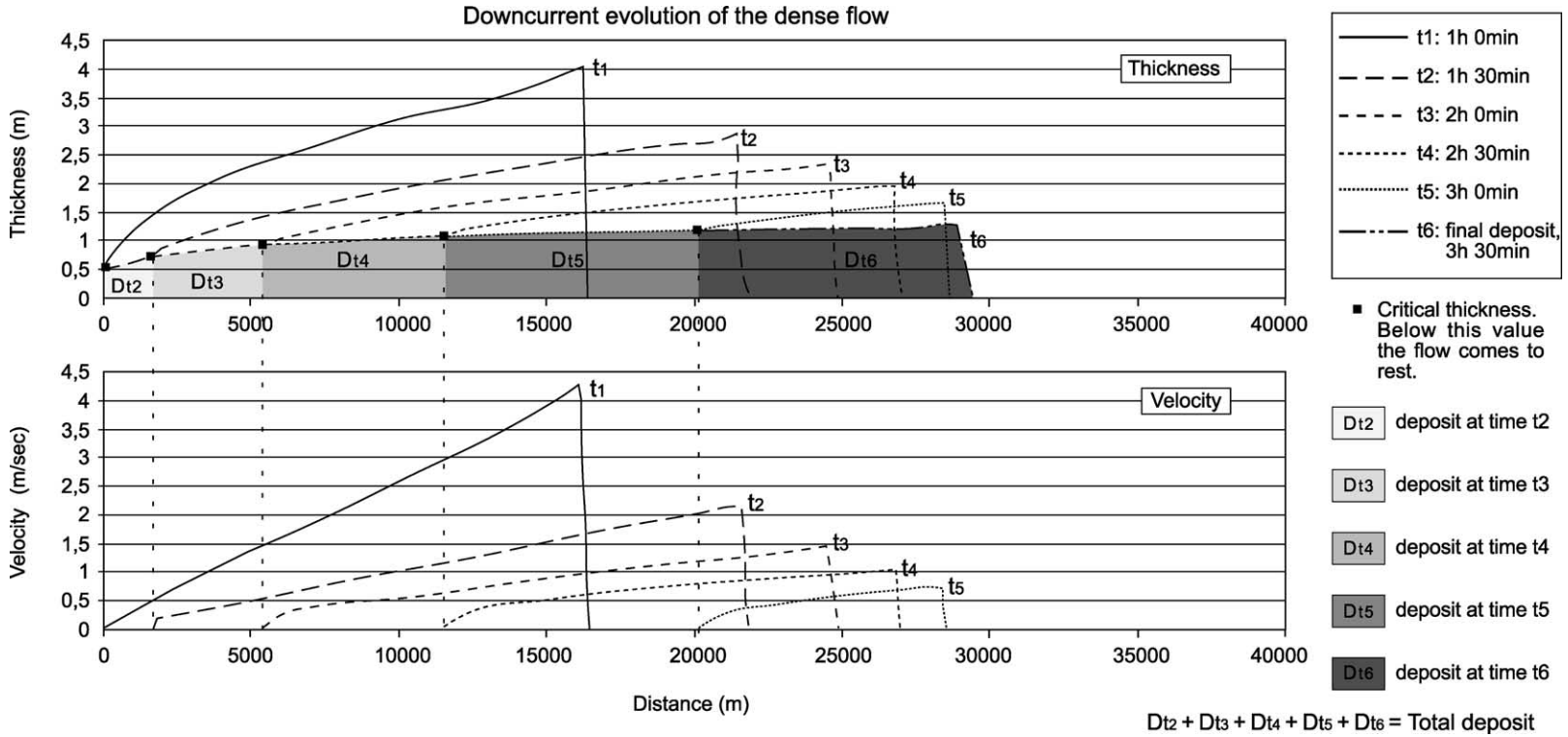

Fig. 15. Diagram showing the downcurrent evolution of the dense flow resulting from the run of the DENS_FLOW code. Flow thickness and velocity profiles as well as the geometry of the related deposit (Dt2–Dt6) are represented at different time steps (t1–t6). The figure points out the importance of a critical thickness value, below which the flow, responsible for F5 deposition, comes to rest (flow velocity equal to zero).

the dense flow comes to rest when its thickness drops below a determined value. As mentioned above, this phenomenon would give emphasis to the flow thickness as controlling factors for the generation and maintenance of the excess pore pressure in dense flows and so influencing their runout distances.

6. Summary and conclusions

The first results of a research project aimed to provide a 2D numerical model simulating the facies tract related to individual subaqueous bipartite flows are presented.

The work is built on a methodology which integrates field-based genetic facies tract analysis, laboratory grain-size analysis and mathematical models. Genetic facies tract analysis of outcropping ancient turbidite systems provides strong sedimentologic input for the numerical model, mainly in terms of inferred process/deposit relationships. On the other hand, assumptions must be made in order to estimate physical and morphologic parameters of the parent flow and of original sedimentary basin. However, in the opinion of the authors, such an approach may strongly improve the reliability of the numerical models dealing with subaqueous gravity flows and also help to give insight into transport and depositional processes of still poorly understood turbidite facies. The main results of the present study are listed below.

1. A new code simulating processes and deposits of dense overpressured flows (DENS_FLOW) has been implemented and coupled with a code simulating processes and deposits of turbulent flows (TURB_FLOW). The resulting code represents the first attempt to simulate the downcurrent evolution of a bipartite flow, through a numerical model based on field constraints derived by a detailed facies analysis (Figs. 2 and 9, Broto turbidite system, Eocene of the south-central Pyrenees).
2. The coupled model is able to correctly reproduce the dense and turbulent flow characteristics both in terms of processes and deposits. In particular, the most remarkable results are the ability of the code to respect the distances travelled by the flow (Fig. 9) and to calculate grain-size distributions directly comparable to the field data (Figs. 12 and 13).
3. As described in Section 3, the basal dense flow behaves as an overpressured flow which progressively undergoes fluidisation and, therefore, deposits graded beds. Taking into account the experimental fluidisation curves of Fig. 5 during the implementation of the physical model, it has been possible to obtain a code able to reproduce with accuracy the vertical grain-size segregation common to many F5 deposits (Fig. 14).
4. With regards to the dynamics of the basal dense flow, Fig. 15 clearly shows how the dense flow comes to rest when its thickness drops below a well-determined value. This is in agreement with the concepts introduced in Section 3.2 in which the thickness of the dense flow is considered to be one of the most important factors controlling the runout distance.
5. Given that the evolution of a bipartite flow can be subdivided in three main dynamic phases (Section 3), the model fails in reproducing the transitional processes and deposits occurring between the dense and turbulent flow phases. Nevertheless, the volume and the grain-size populations resulting from the run of the DENS_FLOW code actually compare to the total volume and grain-size populations of facies F5, F7 and F8 as observed in the field (see Fig. 16 and compare to Fig. 11a). This means that the model is not able to separate the transitional facies (F7 and F8) from those strictly related to the dense flow (F5), which mainly depends on the inability to simulate the transformation of the head of the dense flow. Furthermore, the TURB_FLOW code is able to transport only the finer grain-size populations (very-fine sand to clay), characterising the F9 facies, but it does not keep larger grain sizes in suspension. Regarding this point, we emphasize the importance of the agreement with the experimental data of Mohrig and Marr (2003), which demonstrate how the affiliated turbulent flow derived from the transformation of moderately coherent debris flow is unable to sustain the grain-size population larger than very-fine sand.

In this way, model results reinforce the sedimentologic interpretation given in Section 3 that facies F7 and F8 are related to the downcurrent transformation of the leading edge of the basal dense flow into a turbulent flow. This process gives rise to a relatively dense near-bed suspension, mainly involving medium and coarse-grained sand, in which the characteristic particle support mechanisms of both dense and turbulent flows can coexist.

In order to verify the above assumptions, an additional check has been made. Fig. 17 shows the comparison between the grain-size populations of two field samples, collected within facies F7 and F8 (see Fig. 9 for location), and the grain-size distributions of two parts

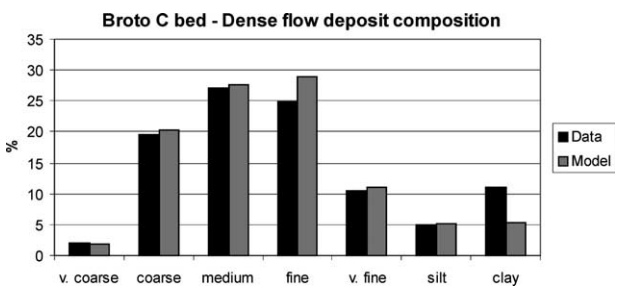

Fig. 16. Comparison between simulated and measured grain-size composition for the dense flow deposits. Note, the simulated deposit accounts for the combined grain-size composition of F5, F7 and F8 facies (Model). Therefore, the grain-size distribution for the corresponding facies sampled in the field (Data), (Fig. 9) were similarly averaged.

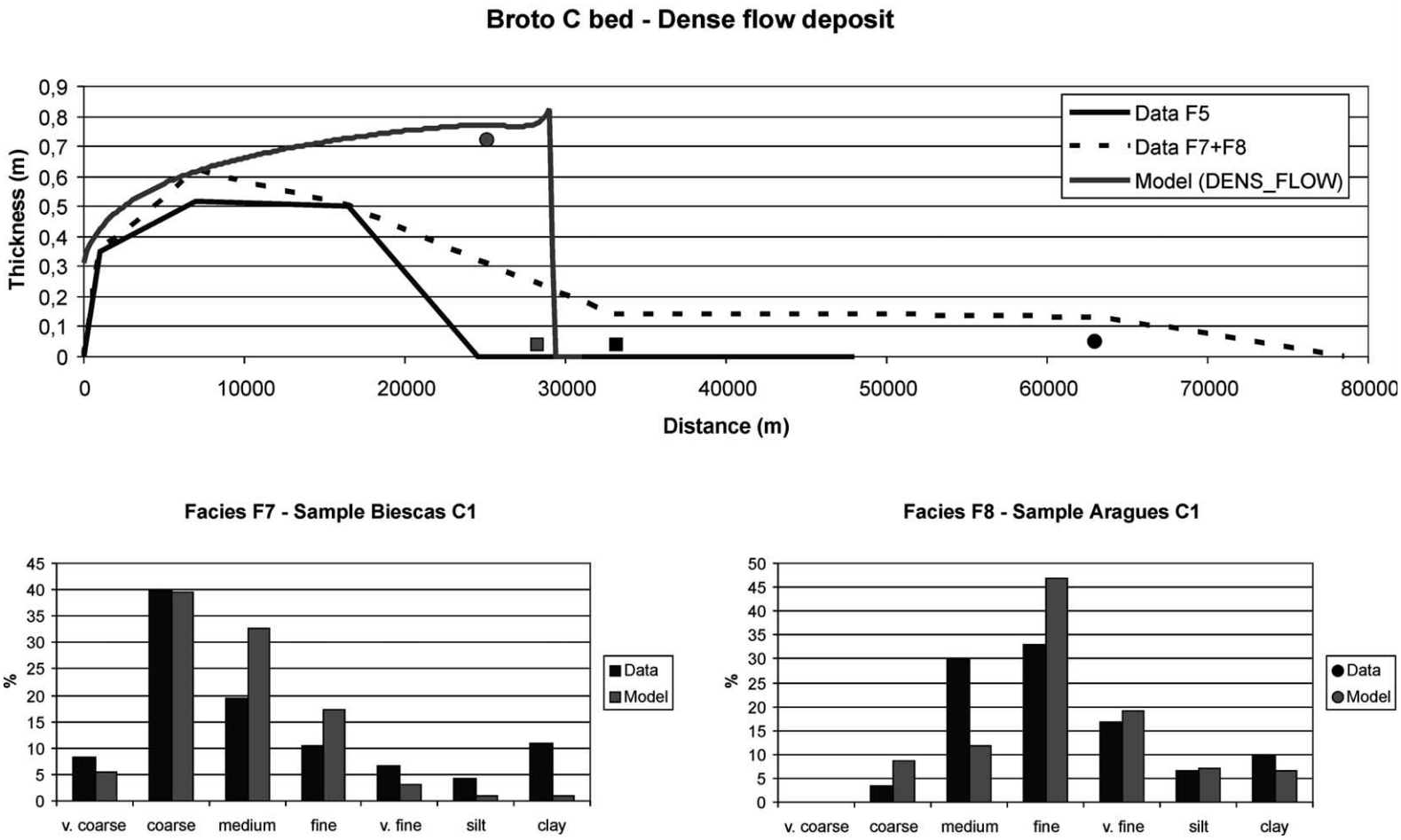

Fig. 17. Comparison between simulated and measured grain-size distributions for samples belonging to facies F7 and F8. In the upper part of the figure the location of both field and modelled samples are indicated. *Facies F7*: (■) field data (sample Biescas C1), (▩) model. *Facies F8*: (●) field data (sample Aragues C1), (◍) model.

of the DENS_FLOW model from which the F7 and F8 deposits, are supposed to originate, through the head flow transformation. In particular, samples Biescas C1 and Aragues C1 are compared to the lower and the upper frontal parts of the model, respectively. In both cases the results show an impressive accordance between field and modelled data, indicating that facies F7 and F8 could be probably modelled by a code able to simulate the reworking of the frontal part of the DENS_FLOW deposit. It is suggested that this item could be approached implementing a bed load transport model which accounts for the part of the near-bed suspension dragged by the turbulent flow.

6. The DENS_FLOW code can probably be very effective in simulating low efficiency flows that, being not able to develop good transformation at the head of the dense flow, deposit mainly F5 facies and poorly developed F9 facies. Moreover, because of the physical model on which it is based, the DENS_FLOW code could probably also satisfactorily reproduce the coarsest facies of the dense flow, i.e. the F2 and F3 facies (Fig. 3).

Acknowledgements

The authors thank ENI for the financial support: (ENI-Exploration and Production Division internal research project GSIS-98-3 and Snamprogetti project 'Deep Water Submarine Pipeline', partially financed by ENI FUND N0 25) and for the permission to publish the results of the study. Eduard Remacha is thanked for providing the high-resolution stratigraphic framework of the Broto turbidite system and for his availability in the field during the sampling campaign in the south central Pyrenees. Flavio Gilardoni and Michele Impalà carried out the sampling and managed the samples at the ENI Laboratories. Luca Mauri performed the grain-size analyses. We also thank Andrea Ortenzi for the petrographic analyses on thin section and for the helpful discussions about grain size and porosity. Stefano Angella and Ferran Bolano are thanked for the helpful discussion in the field. Finally the authors would like to acknowledge the reviews and suggestions of David Mohrig and an anonymous reviewer, which improved the final version of the paper. Jesse Melick and Paola Giaj Via read the manuscript for the English.

References

Allen, J. R. L. (1982) (*Vol. II*). *Sedimentary structures: Their character and physical basis*, Amsterdam: Elsevier, p. 663.

Allen, J. R. L., & Leeder, M. R. (1980). Criteria for the instability of upper-stage plane beds. *Sedimentology*, *27*, 209–217.

Arnott, R. W., & Hand, B. M. (1989). Bedforms, primary structures and grain fabric in the presence of suspended sediment rain. *Journal Sedimentary Petrology*, *59*, 1062–1069.

Baas, J. H., & Best, J. (2002). Turbulence modulation in clay-rich sediment-laden flows and some implications for sediment deposition. *Journal Sedimentary Research*, *72*, 336–340.

Banerjee, I. (1977). Experimental study on the effect of deceleration on the vertical sequence of sedimentary structures in silty sediments. *Journal Sedimentary Petrology*, *47*, 771–783.

Bouma, A. H. (1962). *Sedimentology of some flysch deposits, a graphic approach to facies interpretation*. New York: Elsevier, p. 168.

Campbell, C. V. (1967). Lamina, laminaset, bed and bedset. *Sedimentology*, *8*, 7–26.

Carslaw, H. S., & Jaeger, J. C. (1959). *Conduction of heat in solids* (2nd ed.). Oxford: Oxford University Press, p. 510.

Chen, C.-l. (1997). Debris flow hazards mitigation: mechanics, prediction, and assessment. *ASCE American Society of Civil Engineers, New York*, 817.

Drago, M. (2002). A coupled debris flow–turbidity current model. *Ocean Engineering*, *29*(14), 1769–1780.

Drago, M., & Terenzi, A (2001). Mass gravity flow modelling. In *Proceedings of the 11th ISOPE conference, Stavanger, Norway, 2* (pp. 166–172).

Druitt, T. H. (1995). Settling behaviour of concentrated dispersions and some volcanological applications. *Journal Volcanology Geothermal Research*, *65*, 27–39.

Fair, G. M., & Hatch, L. P. (1933). Fundamental factors governing the streamline flow of water through sand. *Journal American Water Works Association*, *25*, 1551–1565.

Felix, M. (2001). A two-dimensional numerical model for a turbidity current. In B. McCaffrey, B. Kneller, & J. Peakall (Eds.), *Particulate gravity currents* (pp. 71–81). *IAS special publication no. 31*, Oxford: Blackwell.

Felix, M. (2002). Flow structure of turbidity currents. *Sedimentology*, *49*, 397–419.

Fisher, R. V. (1983). Flow transformations in sediment gravity flows. *Geology*, *11*, 273–274.

Freundt, A., & Bursik, M. (1998). Pyroclastic flow transport mechanisms. In A. Freundt, & M. Rosi (Eds.), *From magma to tephra. Modelling physical processes of explosive volcanic eruptions* (pp. 173–245). *Developments in volcanology, 4*, New York: Elsevier.

Hampton, M. A. (1979). Buoyancy in debris flows. *Journal Sedimentary Petrology*, *49*, 753–758.

Imran, J., Harff, P., & Parker, G. (2001). A numerical model of submarine debris flow with graphical user interface. *Computers and Geosciences*, *27*(6), 717–729.

Iverson, R. M. (1997). -The physics of debris flows. *Reviews of Geophysics*, *35*, 245–296.

Iverson, R. M., & Denlinger, R. P. (2001). Flow of variably fluidized granular masses across three-dimensional terrain. 1. Coulomb mixture theory. *Journal of Geophysical Research*, *106*(B1), 537–552.

Jiang, L., & LeBlond, P. H. (1993). Numerical modeling of an underwater Bingham plastic mudslide and the waves which it generates. *Journal of Geophysical Research*, *98*, 10303–10317.

Kneller, B. (1995). Beyond the turbidite paradigm: Physical models for deposition and their implications for reservoir prediction. In A. J. Hartlet, & D. J. Prosser (Eds.), *Characterization of deep marine clastic systems* (pp. 31–49). *Geological Society special publication no. 94*.

Kneller, B. C., & Branney, M. J. (1995). Sustained high-density turbidity currents and the deposition of thick massive sands. *Sedimentology*, *42*, 607–616.

Kneller, B. C., & Buckee, C. (2000). The structure and fluid mechanics of turbidity currents: a review of some recent studies and their geological implication. *Sedimentology*, *47*(Suppl 1), 62–94.

Kunii, D., & Levenspiel, O. (1977). *Fluidization engineering*. New York: Wiley, p. 534.

Liu, K. F., & Mei, C. C. (1989). Slow spreading of a sheet of bingham fluid on an inclined plane. *Journal of Fluid Mechanics*, *207*, 505–529.

Lowe, D. R. (1976). Subaqueous liquified and fluidized sediment flows and their deposits. *Sedimentology*, *23*, 285–308.

Lowe, D. R. (1982). Sediment gravity flow. II. Depositional models with special reference to deposits of high-density turbidity currents. *Journal Sedimentary Research*, *52*, 279–297.

Lowe, D. R., & Guy, M. (2000). Slurry-flow deposits in the Britannia Formation (Lower Cretaceous), North Sea: a new perspective on the turbidity current and debris flow problem. *Sedimentology*, *47*, 31–70.

Major, J. J., & Iverson, M. R. (1999). Debris-flow deposition: effects of pore-fluid pressure and friction concentrated at flow margins. *Geological Society of America Bulletin*, *111*, 1424–1434.

Marr, J. G., Harff, P. A., Shanmugam, G., & Parker, G. (2001). Experiments on subaqueous sandy gravity flows: the role of clay and water content in flow dynamics and depositional structures. *Geological Society of America Bulletin*, *113*, 1377–1386.

McLeod, P., Carey, S., & Sparks, S. J. (1999). Behaviour of particle-laden flows into the ocean: experimental simulation and geological implications. *Sedimentology*, *46*, 523–536.

Mellor, G. L., & Yamada, T. (1982). Development of a turbulence closure model for geophysical fluid problems. *Reviews of Geophysics and Space Physics*, *20*(4), 851–875.

Middleton, G. V. (1993). Sediment deposition from turbidity currents. *Annual Review of Earth and Planetary Sciences*, *21*, 89–114.

Middleton, G. V., & Hampton, M. A. (1973). Sediment gravity flows: Mechanics of flow and deposition. In G. V. Middleton, & A. H. Bouma (Eds.), *Turbidites and deep water sedimentation* (pp. 1–38). *Society of Economic Paleontologists and Mineralogists, Pacific section. Short course lecture notes no. 1*.

Milliman, J. D., & Syvitski, J. P. M. (1992). Geomophic/tectonic control of sediment discharges to the ocean: the importance of small mountains rivers. *Journal of Geology*, *100*, 525–544.

Mohrig, D., & Marr, J. G (2003). Constraining the efficiency of turbidity-current generation from submarine slides, slumps and debris flows using laboratory experiments. *Journal of Marine and Petroleum Geology* (this issue), doi:10.1016/S0264-8172(03)00119-3.

Mohrig, D., Whipple, K. X., Hondzo, M., Ellis, C., & Parker, G. (1998). Hydroplaning of subaqueous debris flows. *Geological Society of America Bulletin*, *110*, 387–394.

Mulder, T., Savoye, B., & Syvitski, J. P. M. (1997). Numerical modelling of a mid-sized gravity flow: the 1979 Nice turbidity current (dynamics, processes, sediment budget and seafloor impact). *Sedimentology*, *44*, 305–326.

Mulder, T., & Syvitski, J. P. M. (1995). Turbidity currents generated at river mouths during exceptional discharges to the world oceans. *Journal of Geology*, *103*, 285–299.

Mulder, T., Syvitski, J. P. M., & Skene, K. I. (1998). Modeling of erosion and deposition of turbidity currents generated at river mouths. *Journal Sedimentary Research*, *68*, 124–137.

Mutti, E. (1971). *An approach to turbidite-facies analysis*. Houston: Esso Production Research Company, EPR-E, p. 63.

Mutti, E. (1992). *Turbidite sandstones*. San Donato Milanese: AGIP, Istituto di Geologia, Università di Parma, p. 275.

Mutti, E., Davoli, G., Tinterri, R., & Zavala, C. (1996). The importance of fluvio-deltaic systems dominated by catastrophic flooding in tectonically active basins. *Memorie di Scienze Geologiche (Padova)*, *48*, 233–291.

Mutti, E., Remacha, E., Sgavetti, M., Rosell, J., Valloni, R., & Zamorano, M. (1985). Stratigraphy and facies characteristics of the Eocene Echo Group turbidite systems, south central Pyrenees. In M. D. Mila, & J. Rosell (Eds.), *IAS sixth European regional meeting, Lleida, field trip 12 guidebook* (pp. 519–576).

Mutti, E., Seguret, M., & Sgavetti, M. (1988). Sedimentation and deformation in the tertiary sequences of the southern Pyrenees. *AAPG Mediterranean Basins Conference, Special Publication University of Parma*, 153.

Mutti, E., Tinterri, R., Benevelli, G., di Biase, D., & Cavanna, G (2003). Deltaic mixed and turbidite sedimentation of ancient foreland basins. *Journal of Marine and Petroleum Geology* (this issue), doi:10.1016/S0264-8172(03)00122-3.

Mutti, E., Tinterri, R., di Biase, D., Fava, L., Mavilla, N., Angella, S., & Calabrese, L. (2000). Delta-front facies associations of ancient flood-dominated fluvio-deltaic systems. *Review of the Society of Geology Espana*, *13*(2), 165–190.

Mutti, E., Tinterri, R., Remacha, E., Mavilla, N., Angella, S., & Fava, L. (1999). An introduction to the analysis of ancient turbidite basins from an outcrop perspective. *AAPG Continuing Education Course Note Series No. 39*, 61.

Nichols, R. J., Sparks, R. S. J., & Wilson, C. J. N. (1994). Experimental studies of the fluidization of layered sediments and the formation of fluid escape structures. *Sedimentology*, *41*, 233–253.

Norem, H., Locat, J., & Schieldrop, B. (1990). An approach to the physics and the modelling of submarine flowslides. *Marine Geotechnology*, *9*, 93–111.

Normark, W. R., & Piper, D. J. (1991). Initiation processes and flow evolution of turbidity currents: Implication for the depositional record. In G. V. Middleton (Ed.), *From shoreline to abyss* (pp. 207–230). *Society of Economic Paleontologists and Mineralogists, special publication no. 46*.

Parsons, J. D., Whipple, K. X., & Simoni, A. (2001). Experimental study of the grain-flow, fluid-mud transition in debris flows. *Journal of Geology*, *109*(4), 427–448.

Peakall, J., Felix, M., McCaffrey, B., & Kneller, B. (2001). Particulate gravity currents: Perspectives. In B. McCaffrey, B. Kneller, & J. Peakall (Eds.), *Particulate gravity currents* (pp. 1–8). *IAS special publication no. 31*, Oxford: Blackwell.

Postma, G., Nemec, W., & Kleinsphein, K. (1988). Large floating clasts in turbidites: A mechanism for their emplacement. *Sedimentary Geology*, *58*, 47–61.

Pratson, L. F., Imran, J., Hutton, E. W. H., Parker, G., & Syvitsky, J. P. M. (2001). BANG1D: a one-dimensional, Lagrangian model of subaqueous turbid surges. *Computers and Geosciences*, *27*(6), 701–716.

Ravenne, C., & Beghin, P. (1983). Apport des experiences en canal a l'interpretation sedimentologique des depots de cones detritiques sous-marins. *Revue de l'Instute Français du Petrole*, *38*(3), 279–297.

Reed, C. W., Niedoroda, A. W., Dalton, C., & Parker, G (2000). Predicting turbidity current speeds using numerical models. *Proceedings of the 19th OMAE conference, New Orleans, Louisiana*, OMAE2000/PIPE-5.

Remacha, E (1983). *'Sand tongues' de la unidad de Broto (Grupo de Hecho), entre el Anticlinal de Boltanay el Rio Osia (Prov. De Huesca)*. PhD thesis. Universidad Autònoma de Barcelona, Facultad de Ciencias, p. 163.

Remacha, E., & Fernàndez, L. P (2003). High-resolution correlation patterns in the turbidite systems of the Hecho Group, south-central Pyrenees, Spain. *Journal of Marine and Petroleum Geology* (this issue), doi:10.1016/S0264-8172(03)00137-5.

Remacha, E., Fernàndez, L. P., Maestro, E., Oms, O., Estrada, R., & Teixell, A. (1998). The upper Hecho Group turbidites and their vertical evolution to deltas (Eocene south-central Pyrenees) (complementary information to field trip a guidebook). In A. Melendez Hevia, & A. R. Soria (Eds.), *15th international sedimentological congress (IAS), April 8–12, excursion guidebook* (pp. 21Universidad Autònoma de Barcelona and Universidad de Oviedo.

Richardson, Y. F., & Zaki, W. N. (1954). Sedimentation and fluidization, Part I. *Transactions of the Institute of Chemical Engineering*, *32*, 35–53.

Rodi, W. (1980). *Turbulence models and their applications in hydraulics. State of the art paper*. Delft, The Netherlands: IAHR, p. 104.

Sanders, J. E. (1965). Primary sedimentary structures formed by turbidity currents and related resedimentation mechanisms. In G. V. Middleton (Ed.), *Primary sedimentary structures and their hydrodynamic interpretation* (pp. 192–219). *Society of Economic Paleontologists and Mineralogists special publication no. 12*.

Shanmugam, G. (2000). 50 years of the turbidite paradigm (1950s–1990s): deep-water processes and facies models: a critical perspective. *Marine and Petroleum Geology*, *17*, 285–342.

Simpson, J. E. (1997). *Gravity currents in the environment and the laboratory* (2nd ed.), p. 244.

Sparks, R. S. J. (1976). Grain size variations in ignimbrites and implications for the transport of pyroclastic flows. *Sedimentology*, *23*, 147–188.

Takahashi, T. (1991). *Debris flow*. *IAHR\AIRH monograph series*, Rotterdam: A.A. Balkema, p. 165.

Takahashi, T. (2001). Mechanics and simulation of snow avalanches, pyroclastic flows and debris flow. In B. McCaffrey, B. Kneller, & J. Peakall (Eds.), *Particulate gravity currents* (pp. 11–43). *IAS special publication no. 31*, Oxford: Blackwell.

Tinterri, R., & Consonni, A. (2001). Dimensional analysis applied to the facies analysis of gravity flow deposits. In U. G. Wortmann, & H. Funk (Eds.), *21st IAS meeting of sedimentology, 3–5 September 2001, Davos (Switzerland), abstracts book (poster section)* (pp. 204).

Van Rijn, L. C (1989). *Sediment transport by currents and waves*. Delft hydraulics, report H 461.

Vrolijk, P. J., & Southard, J. B. (1997). Experiments on rapid deposition of sand from high-velocity flows. *Geoscience Canada*, *24*, 45–54.

Wilson, C. J. N. (1984). The role of fluidization in the emplacement of pyroclastic flows. 2. Experimental results and their interpretation. *Journal Volcanology Geothermal Research*, *20*, 55–84.

Zeng, J., & Lowe, D. R. (1997a). Numerical simulation of turbidity current flow and sedimentation. I. Theory. *Sedimentology*, *44*, 67–84.

Zeng, J., & Lowe, D. R. (1997b). Numerical simulation of turbidity current flow and sedimentation. II. Results and geological applications. *Sedimentology*, *44*, 85–104.